LBL-31735
UC-404
Preprint

Lawrence Berkeley Laboratory
UNIVERSITY OF CALIFORNIA

Materials Sciences Division

Submitted to Surface Science

X-Ray Photoelectron Diffraction and Low Energy Electron Diffraction Study of the Interaction of Oxygen with the Ni(001) Surface: c(2x2) to Saturated Oxide

R.S. Saiki, A.P. Kaduwela, M. Sagurton, J. Osterwalder, D.J. Friedman, C.S. Fadley, and C.R. Brundle

September 1992

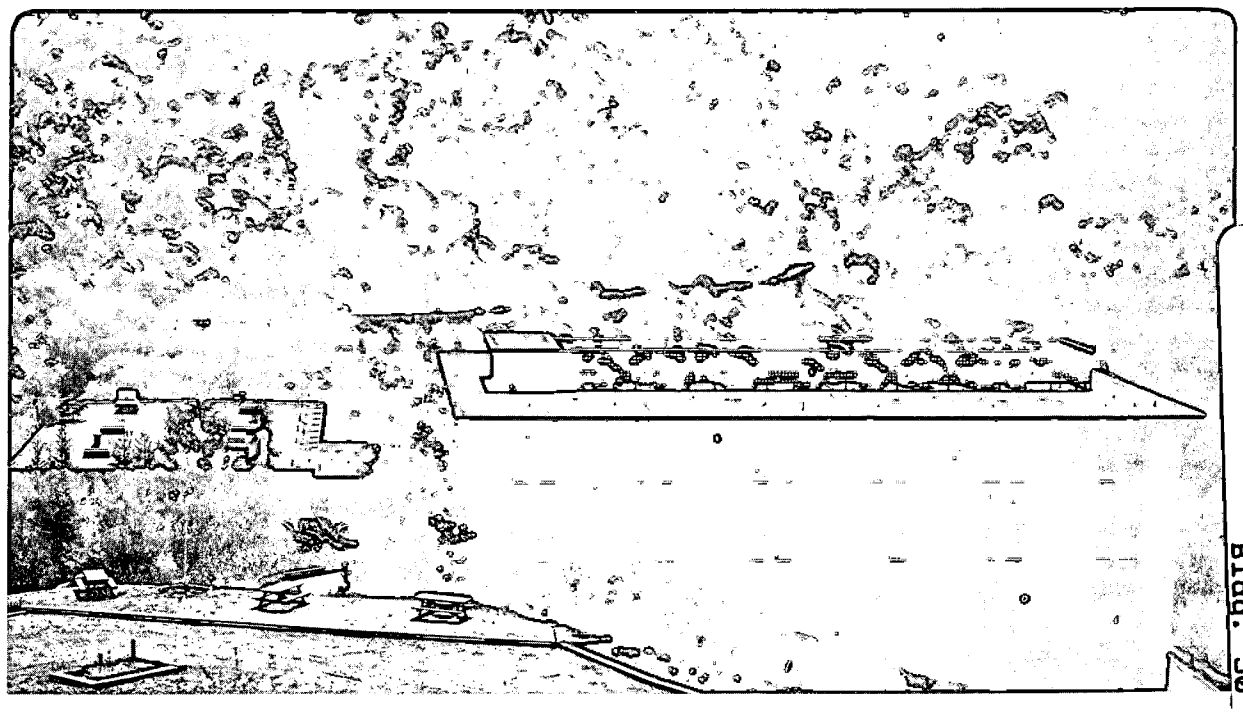

Prepared for the U.S. Department of Energy under Contract Number DE-AC03-76SF00098

DISCLAIMER

LBL-31735
UC-404

X-RAY PHOTOELECTRON DIFFRACTION AND LOW ENERGY ELECTRON DIFFRACTION STUDY OF THE INTERACTION OF OXYGEN WITH THE Ni(001) SURFACE: c(2X2) TO SATURATED OXIDE

R.S. Saiki,[*] A.P. Kaduwela,[*] M. Sagurton,[*] J. Osterwalder,[*] D.J. Friedman ,[*]
C.S. Fadley,[*†] and C.R. Brundle[§]

[*]Department of Chemistry
University of Hawaii
Honolulu, HI 96822 USA

[†]Materials Sciences Divsion
Lawrence Berkeley Laboratory
University of California
Berkeley, CA 94720 USA

[§]IBM Research
Almaden
San Jose, CA 95120 USA

September 1992

This work was supported by the National Science Foundation under Grants CHE80-21355 and CHE83-20200, by the Office of Naval Research under Contracts N00014-87-K-0512 and N00014-90-5-1457, and by the Director, Office of Energy Research, Office of Basic Energy Sciences, Materials Sciences Division, of the U.S. Department of Energy under Contract No. DE-AC03-76SF00098.

(Submitted to Surface Science)

X-ray Photoelectron Diffraction and Low Energy Electron Diffraction Study of the Interaction of Oxygen with the Ni (001) Surface: c(2x2) to Saturated Oxide

R.S. Saiki, A.P. Kaduwela[†], M. Sagurton[‡], J. Osterwalder[*], D.J. Friedman[††], C.S. Fadley[†,**]

Department of Chemistry, University of Hawaii, Honolulu, Hawaii 96822 USA

and C.R. Brundle

IBM Research, Almaden, San Jose, California 95120 USA

Abstract

We have carried out a combined x-ray photoelectron diffraction (XPD) and low-energy electron diffraction (LEED) study of the interaction of oxygen with Ni(001) at ambient temperature from the c(2×2) structure up to the saturated oxide. Several new conclusions are possible based on an R-factor comparison of an extensive series of azimuthal- and polar- O 1s XPD data to theoretical simulations based on a single-scattering cluster (SSC) model with spherical wave scattering. A new method for normalizing experimental and theoretical intensities for XPD R-factor analyses is also used. For the c(2×2) structure, we find that the oxygen sits in the fourfold hollow site, at a vertical distance (z) of approximately 0.75 Å above the first Ni plane, in excellent agreement with several prior studies. There is also strong evidence from the XPD results that oxide nucleation occurs very early in the chemisorption region and this effect could explain the proposals for in-plane bonding or pseudobridge bonding previously reported in the literature. The saturated oxide that forms at ambient temperatures is found from LEED and XPD to form a highly strained superlattice that is expanded by $^1/_6$ with respect to the

underlying Ni(001). We also find that the saturation oxide coverage is much larger than that previously reported in the literature of 2–3 monolayers (ML), and that it is in fact 4–5 ML. Other qualitative conclusions concerning the nature of the strain in the oxide are also possible.

1. INTRODUCTION:

Despite being the object of intensive investigation by a variety of surface-structure techniques over the past 20 years, there is still much to be learned about the exact nature of the various structures that arise on the Ni(001) surface when it is exposed to oxygen [1–18]. In order to better understand this system, we have obtained an extensive set of both polar- and azimuthal-x-ray photoelectron diffraction (XPD) data, as well as low energy electron diffraction (LEED) observations, at a number of different oxygen coverages. Of particular interest was determining the geometric structures of both the c(2×2) structure and of the saturated oxide overlayer that grow at ambient temperature (~300 K) on this surface, and in assessing the degree of coexistence of these two structures. XPD has been shown to be very useful in deducing structural information from ordered adsorbate atoms lying in or near the surface plane or from thin epitaxial films on a substrate, especially at kinetic energies in the range of 500–1500 eV [19, 20]. XPD is also in comparison to LEED more of a short-range order probe (~25–50 Å range compared to ~100–200 Å for the latter). Photoelectron diffraction data at such high energies have furthermore been successfully analyzed using simple single scattering cluster (SSC) calculations to differentiate between the various proposed surface structures thought to be be present [19, 20]. In order to better quantify the degree of agreement between experiment and theory, we have also used an R-factor analysis.

We begin by introducing the main features of the O/Ni(001) system as known previously. It has been well established that the adsorption of oxygen on Ni(001) occurs in four major steps at ambient temperature [1], with a schematic of some of the structures involved being shown in Figure 1:

(i) Rapid submonolayer adsorption with no disruption of the crystal lattice in the surface region, first leading to an ordered p(2×2) and then a c(2×2) overlayer geometry that would have ideal coverages of $\Theta = 0.25$ and 0.50 monolayers (ML), respectively. We will here restrict our consideration to the c(2×2) structure, whose completion is schematically indicated in Figure 1(a).

(ii) Initiation of a c(2×2) plateau, the width of which is highly dependent on the quality of the Ni(001) surface and on the substrate temperature. This plateau is thought to be due to the complete filling in of all remaining available sites for dissociation of the impinging oxygen molecules and subsequent chemisorption. The best c(2×2) overlayer has been observed experimentally at coverages in the range of 0.30–0.40 ML, or somewhat below the ideal coverage.

(iii) Penetration of oxygen into the Ni lattice resulting in the development of isolated NiO nuclei or islands, accompanied by a rapid upswing in the oxygen sticking coefficient at coverages greater than ~0.50 ML. With increasing oxygen exposures, these NiO islands grow predominantly, but not necessarily exclusively, in the (001) orientation. Here, oxide clearly coexists with the c(2×2) structure.

(iv) Saturation occurs when these islands coalesce at a coverage that has been estimated previously to be in the range of 2–4 ML of NiO [Figure 1(d)]. The characteristics of the saturated layer are dependent on the actual mixture of two distinct oxide epitaxial orientations thought to be present, specifically in the [001] and [111] orientation, and this mixture is in turn dependent on the substrate temperature during exposure [14].

There also exists a very slow, diffusion-limited, vertical oxide growth on significantly higher oxygen exposures that is known as the "tarnishing" region.

At low oxygen coverages ($\Theta < 0.5$ ML), there has been considerable controversy over the actual geometric positions of the oxygen atoms in the c(2×2) overlayer. Part of this problem can be traced back to a misunderstanding of the effect annealing has on the surface structure. Crystal annealing was carried out in some older studies primarily to sharpen and intensify the LEED spots associated with the overlayer. However, at temperatures as low as 450–600 K, annealing can cause atomic oxygen initially chemisorbed onto the surface to diffuse into the crystal bulk and possibly also to form oxide nuclei, thus interfering with the ensuing structural determination [1]. Simple inward diffusion should not be confused with oxide nucleation however. In the early 1980's, an XPD study by our group [5] suggested that the oxygen overlayer resided in the same plane as the topmost Ni layer for an oxygen coverage approaching 0.5 ML, the theoretical limit for an ideal c(2×2)O structure; in this work however, it was pointed out that the XPD patterns would be very sensitive to the presence of small oxide nuclei, an effect which could have biased the results towards an in-plane geometry [5]. The in-plane geometry was in conflict with an earlier LEED analysis by Demuth *et al.* [2] who originally proposed that the p(2×2) and c(2×2) overlayer structures had the same *z*-distance of 0.8 Å. A subsequent theoretical study by Upton and Goddard [7], however, supported the short Ni–O bond distance and initiated the "oxide state" controversy for the c(2×2) overlayer. In a subsequent LEED study by Tong *et al.* [8], the possibility that the oxygen overlayer resided in the same plane as the topmost Ni layer could not be differentiated from a situation where the oxygen atoms sat well above the surface at a distance of 0.8 Å. Stöhr *et al.* [9] used surface extended x-ray adsorption fine structure (SEXAFS) to rule out the in-plane bonding site and found that both the p(2×2) and c(2×2) structures occupied the fourfold hollow sites and had identical *z*-distances of 0.86 Å. In a followup LEED study, Demuth *et al.* [10] however, suggested that the c(2×2)

structure had a *z*-distance of 0.80 Å, but more importantly, that the oxygen atoms were displaced 0.3 Å from the fourfold hollow site along the <110>-directions. This was described as being the pseudobridge bonding site. Such an unusual displacement was claimed to be entirely consistent with an observed broadening of several of the peaks associated with scattering off of nearest neighboring Ni atoms in the χ-curves of the SEXAFS analysis. However in the most recent LEED analysis of this system [15], a multilayer, tensor approach has shown that the preferred structure has the oxygen atoms residing once again in the fourfold hollow sites, although at a somewhat shorter *z*-distance of 0.75 Å. We will present a new and more detailed XPD analysis of the c(2×2) structure in this paper.

Although the interaction of oxygen with the Ni(001) surface at higher coverages (> 0.5 ML) is known to result in the onset of oxide nucleation and growth, it has also been concluded that the onset of oxide nucleation occurs well before the cessation of c(2×2) formation [1]. However there is very little prior quantitative information concerning the relative amounts of oxygen in the c(2×2) and oxide structures. The actual oxidation of the Ni(001) surface is a remarkably complex interaction that is highly dependent on the temperature of the substrate during the oxygen exposure. In an earlier XPD/LEED paper on this system [13], Saiki *et al.* reported LEED observations of a (6×6) NiO(001) centered-square superlattice formation which grows on a (7×7) Ni(001) mesh, and that this coexists with two orientations of a minority NiO(111) species rotated 30° apart from each other and manifesting themselves as a 12-spot ring when viewed by LEED. (Various LEED photographs relevant to this discussion have previously been published in Reference 13). These two co-existent oxide phases were first discussed by Holloway and Hudson [3] and first hypothesized to be NiO(001) and NiO(111) by Mitchell *et al.* [4]. Subsequent work by Wang *et al.* [14] has shown that room temperature is actually a crossover point for the formation of the (111) versus (100) orientations of NiO. At lower temperatures, NiO(111)

is the majority species while the more stable (100) orientation is observed at room temperature and above. Although the (111) structure is clearly seen in our ambient temperature LEED pattern, it yields no observable peaks in the XPD curves, and has thus been estimated to comprise about 5% and no more than 10% of the total saturated oxide [13].

Annealing the saturated oxide for a few minutes to as little as 523 K results in the removal of both the NiO(111) 12-spot ring and the centered-square spot splitting of the superlattice, and also leads to the reappearance of a similar c(2×2) structure that is observed at lower oxygen coverages [13, 14]. This is postulated to be due to the formation of oxygen-rich and oxygen-depleted regions, as illustrated in Figure 1(e). The oxygen-rich regions appear to have greater order in the vertical direction that could be the result of the creation of a significantly thicker oxide layer. The LEED spots of NiO(001) after annealing are more intense, but remain centered very near their previous position and are rather diffuse, which suggests that the annealed oxide is still under considerable strain and/or exists in rather small domains. The oxygen-poor regions are thought to be covered by a c(2×2) oxygen overlayer that leads to the recovery of a c(2×2) structure in LEED after annealing.

The formation of two or more monolayers of ordered NiO(001) should result in significant modulations of the O 1s x-ray photoelectron spectroscopy (XPS) signal, similar to that expected from a single-crystal of NiO. In the prior XPD analysis of the annealed oxide layer [13], it was determined that the best fit of theoretical calculations to high-angular resolution O 1s azimuthal XPD data at takeoff angles θ of 35.3° and 45.0° with respect to the surface occurred for a large NiO(001) cluster 2-ML thick that covered an area of approximately 20 Å in radius from the emitting oxygen atom. This cluster had a lattice constant expanded by $^1/_6$ over bulk Ni, that is $a_{NiO} = {}^7/_6(3.52\ \text{Å}) = 4.11\ \text{Å}$, a value determined from measurements of the position of the oxide diffraction spots in LEED.

Annealing does not fully relieve the expansion in the horizontal directions but retains the slight 1.4% compression below the bulk oxide lattice constant of 4.17 Å. However, the annealed oxide had an XPD pattern that was markedly different from the unannealed data, indicating that some type of irreversible structural changes were occurring in the process. These effects also are explored in greater detail in this paper.

In the following sections, we present a more detailed set of XPD results, and these are found to lead to several new conclusions concerning the structures of oxygen on Ni(001).

2. EXPERIMENTAL CONSIDERATIONS:

The two experimental systems used for this study have been described in detail previously [19(a), 21] and consist of Hewlett-Packard (HP) 5950A and VG Scientific ESCALAB5 x-ray photoelectron spectrometers that have been modified for angle-resolved measurements with the installation of high-accuracy two-axis specimen goniometers. The VG system also has a series of angle-defining stainless steel tube arrays mounted in front of the entry lens to the energy analyzer [21]. These tube arrays allow different angular resolutions of ±1.5°, ±3.0°, and ~ ±6.0° (full open) to be selected. Prior studies have shown an increase in the amount of diffraction fine structure when the angular resolution is increased from the standard ~ ±3.5°–±6.0° to the current minimum ±1.5° [21], and that such additional fine structure may be useful in deriving additional details of overlayer structures [19(c), 22]. An unpolarized Al Kα radiation source ($h\nu$ = 1486.6 eV) was used for the primary excitation in either case. The experimental configuration is shown in Figure 2; the angle α between radiation incidence and electron exit was 72° in the HP system and 48° in the VG system. The detector consisted of a Surface Science Laboratories multichannel system on the HP and a single channeltron on the VG spectrometer, although

the latter has subsequently been upgraded to include a similar multichannel detector [23]. Precision scanning of either the ϕ– or θ–electron emission directions was possible under direct computer control. Base pressures were maintained at better than 5×10^{-11} Torr in the main analysis chamber. A LEED unit was available on the HP system to observe the surface symmetry of the various overlayer surface structures that were obtained.

The Ni(001) sample was cut from a single-crystal rod with a low-speed diamond saw and oriented to within $\pm 0.3°$ of the (001) surface as determined by Laue back-scattering measurements. The surface was then mechanically polished with successively finer grades of diamond paste before final chemical etching in a 10% solution of 1:1 nitric/sulfuric acid to remove as much of the surface disorder from mechanical polishing as possible before mounting in the spectrometer. Surface cleanliness and oxygen coverage were monitored by XPS, as described in detail in the next section. The initial and subsequential cleanings were done by successive *in situ* Ar^+ bombardments at 600 volts, followed immediately by annealing to approximately 873 K until the combined coverage of C, O, and S impurities totaled less than 0.02 ML and the LEED pattern showed a sharp p(1×1) pattern of the (001) surface with high contrast.

The oxygen exposures were performed at room temperature, with the oxygen pressure being monitored by a standard Bayard-Alpert ion gauge. The best compromise between the sharpest c(2×2) pattern and the most intense fractional-order spots was observed at an exposure of 30 L (10^{-7} Torr × 300 sec.); this also is found to be the location of the minimum slope in the uptake curve, as shown in Figure 3 and discussed in more detail below. The XPS-based coverages at this exposure were found to be 0.38 ± 0.04 ML, in excellent agreement with prior studies [1]; the determination of these coverages also is discussed below. The saturated-oxide exposure was somewhat arbitrarily set at 1200 L (10^{-5} Torr × 120 sec.), since by this point the oxygen coverage (approximately 2.4 ML as measured with respect to Ni(001) and without correcting for attenuation by the oxide

overlayer, so as to represent a minimum value) did not increase appreciably with significantly larger oxygen exposures [cf., Figure 3(a)]. In either c(2×2)O or the saturated oxide, the O 1s/ Ni $2p_{3/2}$ intensity ratios used for quantitative analysis were taken along directions well away from any strong photoelectron diffraction forward scattering features and also chosen so as to represent an average intensity from the surface at a given θ. The individual intensity measurements were found to be very reproducible, with values ranging within ±5% of the values reported in this paper. The importance of such care in these measurements will be explained later.

The precise calibration of the θ– and ϕ–angles with respect to the crystal axes (cf., Figure 2) was done with high angular resolution and using the strong and very narrow Ni $2p_{3/2}$ XPD peaks from the clean surface that occur along the <110> directions. This calibration had an accuracy of ±0.2°. A series of O 1s azimuthal scans (E_{kin} = 954 eV, electron wavelength = 0.40 Å) were taken for both the c(2×2) and saturated oxide structures over a ϕ-range of 380° at grazing takeoff angles with respect to the surface of θ = 8°, 11°, 14°, and 17° to yield enhanced surface sensitivity and at much larger angles near $\theta \approx 35°$ and 45° to probe deeper lying structures. Polar scans were also measured in high-symmetry azimuths. All of this data will be discussed below.

3. THEORETICAL MODELING AND DATA ANALYSIS:

3.1. QUANTITATIVE ANALYSIS OF SURFACE COVERAGES-

The theoretical model used to describe the relationship between the integrated XPS peak intensities and different surface coverages in this study has been described in great detail elsewhere [19]. Basically, it assumes a uniform overlayer that is atomically flat, that the incident x-rays have penetration depths that far exceed the elastic escape depths of the

photoelectrons, that any enhancements of the photocurrent due to diffraction effects from the uniform overlayer/substrate are either negligible or have somehow been averaged over, and that inelastic scattering can be adequately described by a simple exponential in the attenuation length or mean free path (Λ_e). Electron refraction due to the inner potential (V_o) can often be neglected due to the large takeoff angles and/or the high kinetic energies of the photoelectrons being utilized, but we have included it in our calculations for completeness.

For a bulk solid having little or no local order to produce diffraction, the relationship between the integrated intensity of a core level photoemission peak is given by [19(a)]:

$$I_k = I_o \Omega_o(E_{kin}) A_o(E_{kin}) D_o(E_{kin}) \rho_k \frac{d\sigma_k}{d\Omega} \Lambda_e(E_{kin}) \ ,$$

where I_o is the intensity of the incident monochromatic x-ray flux, $\Omega_o(E_{kin})$ is the effective solid angle of the detector, $A_o(E_{kin})$ is effective source area of the sample seen by the analyzer, $D_o(E_{kin})$ is the detector efficiency, ρ_k is the density of the k^{th} species under study, $\frac{d\sigma_k}{d\Omega}$ is the differential cross-section of the peak k under study, and $\Lambda_e(E_{kin})$ is the inelastic attenuation length of the photoelectron in the solid.

XPS peak intensity ratios have been shown to be useful in determining the fractional monolayer coverages of adsorbates and the stochiometric ratios of the various elements present in the near surface region. The purely instrumental parameters I_o, Ω_o, A_o, and D_o will cancel out when intensity ratios of the various chemical species are examined, provided that the kinetic energies are reasonably close. If photoemission peaks with more widely differing energies are studied [as is the case for the O 1s (954 eV) and Ni $2p_{3/2}$-metal (629 eV) considered here], the change in the detector solid angle $\Omega_o(E_{kin})$ with energy can become significant, and suitable values for the particular spectrometers we have used have been tabulated and published [23, 24]. Similarly, the differential cross-sections have also been calculated and tabulated for many cases [25]; the same is true for the electron

attenuation lengths of various solids [26]. The overall accuracy of such measurements are in the range of ±20% at the submonolayer concentration levels and the majority of the error is in the determination of $\Lambda_e(E_{kin})$, which is expected to vary roughly as the square root of the kinetic energy in a given material for the energies of interest here [26].

For the ideal case of a uniformly distributed adsorbate present at submonolayer quantities [the situation for c(2×2)O/Ni(001)], the oxygen coverage can best be determined by assuming that the overlayer is completely non-attenuating [19(a)]. Comparisons of the Ni $2p_{3/2}$ intensities both before and after oxygen exposure to form c(2×2) showed essentially no change in absolute value and this supports our use of the completely non-attenuating overlayer model. The O 1s/ Ni $2p_{3/2}$ (metal) intensity ratio for this dilute overlayer then becomes:

$$\frac{I_{O1s}(954\text{ eV})}{I_{Ni2p(m)}(629\text{ eV})} = \frac{\Omega_O(954\text{ eV})}{\Omega_O(629\text{ eV})} \cdot \frac{\frac{d\sigma_{O1s}}{d\Omega}}{\frac{d\sigma_{Ni2p}}{d\Omega}} \cdot \frac{S'}{\rho_{Ni(m)} \cdot \Lambda_e^m(629\text{ eV}) \cdot \sin\theta} ,$$

where m = metal peak, S' = number of oxygen atoms per cm^2, $\rho_{Ni(m)}$ = atomic density in Ni metal = 9.14×10^{22} atoms/cm^3, and $\Lambda_e^m(629\text{ eV})$ = the mean free path in the metal at 629 eV. This can be rearranged to yield the c(2×2) coverage as:

$$S'[c(2\times2)] = \left[\frac{I_{O1s}}{I_{Ni2p(m)}}\right] \cdot \frac{\Omega_O(629\text{ eV})}{\Omega_O(954\text{ eV})} \cdot \frac{\frac{d\sigma_{Ni2p}}{d\Omega}}{\frac{d\sigma_{O1s}}{d\Omega}} \cdot \rho_{Ni(m)} * \Lambda_e^m(629\text{ eV}) \cdot \sin\theta \ .$$

Substituting in the relevant values,

$\frac{\Omega_O(629\text{ eV})}{\Omega_O(954\text{ eV})} = 1.44$ (as derived previously for the HP spectrometer [24]),

$$\frac{\frac{d\sigma_{Ni2p}}{d\Omega}}{\frac{d\sigma_{O1s}}{d\Omega}} = 4.674 \text{ (calculated from data in Reference 25)},$$

$$\Lambda_e^m(629 \text{ eV}) = 10.0 \times 10^{-8} \text{ cm [from Reference 26(c)]},$$

and $\theta = 45°$, yields the number of monolayers of oxygen present with respect to the Ni(001) surface as:

$$\text{\# ML of O} = \frac{S'[c(2\times2)O]}{S[Ni(001)]} = 27.01 \cdot \left[\frac{I_{O1s}}{I_{Ni2p(m)}}\right], \quad (1)$$

where S[Ni(001)] = the surface density of Ni(001) $= \frac{2 \text{ atoms}}{[a_{o(Ni)}]^2} = 1.61 \times 10^{15}$ atoms/cm^2.

In determining coverages for the saturated oxide, we have measured the Ni $2p_{3/2}$ signal from the clean Ni surface and the O 1s signal from the reacted surface just after exposure; this avoids the considerable difficulties in trying to distinguish the Ni $2p_{3/2}$(metal) and Ni $2p_{3/2}$(oxide) features in nickel spectra for the oxidized case. The overlayer of thickness t_{ox} is now assumed to be isotropically attenuating. The intensity ratio here becomes [19(a)]:

$$\frac{I_{O1s}}{I_{Ni2p(m)}} = \frac{\Omega_o(954 \text{ eV})}{\Omega_o(629 \text{ eV})} \cdot \frac{\rho_{O(ox)}}{\rho_{Ni(m)}} \cdot \frac{\frac{d\sigma_{O1s}}{d\Omega}}{\frac{d\sigma_{Ni2p}}{d\Omega}} \cdot \frac{\Lambda_e^{ox}(954 \text{ eV})}{\Lambda_e^m(629 \text{ eV})} \cdot$$

$$\left[1 - \exp\left(\frac{-t_{ox}}{\Lambda_e^o(954 \text{ eV}) \cdot \sin\theta}\right)\right],$$

which on rearrangement and substitution of the various values, is then:

$$t_{ox} = -\ln\left[1 - \left(C \cdot \frac{I_{O1s}}{I_{Ni2p(m)}}\right)\right] \cdot \Lambda_e^{ox}(954\ eV) \cdot \sin\theta \ ,$$

where:

$$C = \frac{\Omega_o(629eV)}{\Omega_o(954eV)} \cdot \frac{\rho_{Ni(m)}}{\rho_{O(ox)}} \cdot \frac{\frac{d\sigma_{Ni2p}}{d\Omega}}{\frac{d\sigma_{O1s}}{d\Omega}} \cdot \frac{\Lambda_e^m(629eV)}{\Lambda_e^{ox}(954eV)} = 8.641 \ ,$$

$\Lambda_e^o(954\ eV)$ = electron mean free pathlength in the oxide layer, taken in our calculations to be 12.3 Å [26], and

$$\rho_{O(ox)} = \frac{1}{(7/6)^3} \cdot \rho_{Ni(m)} = 5.76 \times 10^{22}\ atoms/cm^3 \ ,$$

as calculated with allowance for the $7/6$ expansion relative to the Ni lattice observed in LEED. Thus we have finally,

$$t_{ox}\ (Å) = -8.72 \cdot \ln\left[1 - 8.641\left(\frac{I_{O1s}}{I_{Ni2p(m)}}\right)\right] . \qquad (2)$$

From the $7/6$ expansion relative to the underlying Ni(001), the oxide surface density becomes,

$$S'[NiO(001)] = \frac{2\ atoms}{[(7/6)(a_{o[Ni]})]^2} = 1.185 \times 10^{15}\ atoms/cm^2$$

and the "unrelaxed" vertical distance between planes is given by:

$$d_{100}(ox) = (1/2)(7/6(a_{o[Ni]})) = 2.054 \text{ Å} \ .$$

From Equation (2), the number of monolayers of oxide with respect to the oxide surface density is then given by:

$$\frac{tox(Å)}{d_{100}(ox)} = -4.25 \bullet \ln\left[1 - 8.641\left(\frac{I_{O1s}}{I_{Ni2p(m)}}\right)\right] ,$$

and the # ML's of oxide with respect to the Ni(001) surface density by:

$$\frac{tox(Å)}{d_{100}(ox)\bullet(7/6)^2} = -3.12 \bullet \ln\left[1 - 8.641\left(\frac{I_{O1s}}{I_{Ni2p(m)}}\right)\right] . \qquad (3)$$

The inelastic attenuation lengths are an important ingredient in any such XPS surface analysis, and we have here used two different approaches to assess the difference they make. In the first approach already indicated above, an experimental value of Λ_e^m(629 eV) = 10.0 Å for propagation in Ni metal was used as a starting point; this has been found to give excellent results for the XPS analysis of the well-defined c(2×2)S overlayer by Connelly *et al.* [26(c)]. We will also see below that it gives a c(2×2)O coverage of 0.38 ML that is in excellent agreement with those from several other methods [1, 18]. As no accurate experimental Λ_e data are available for NiO, the 10.0 Å value for the metal was then scaled simply as $(E_{kin})^{0.52}$ to yield values for the oxide of Λ_e^{ox}(629 eV) = 10.0 Å and Λ_e^{ox}(954 eV) = 12.3 Å. These latter values do not however, take into account the composition and density changes from metal to oxide. As another approach, we have used the equations and tabulations of Penn [27] to determine these values. These do not have a direct experimental calibration, but do take into account the atomic makeup of each material. They yield

Λ_e^m(629 eV) = 8.2 Å, Λ_e^{ox}(629 eV) = 8.6 Å, and Λ_e^{ox}(954 eV) = 11.6 Å, values which are all within 6–21% of those we have used. Since our 10.0 Å value for Λ_e^m(629 eV) has experimental support from prior XPS studies of both c(2×2)S and c(2×2)O, we believe that this is in any case the most reliable value to use. The other two oxide values of 12.3 Å and 11.6 Å that are of relevance here in determining the saturated oxide thickness are very close in the two approaches. If anything, using the slightly lower 11.6 Å value would yield a somewhat thicker saturated oxide layer thickness. Thus, based upon the present state of our knowledge of the attenuation lengths in the oxide, we have used a highly reliable set of values.

Turning now to the actual values derived in this study, we note that the coverage of the c(2×2)O structure at 30 L was determined from the ratio of the O 1s and Ni $2p_{3/2}$ peak areas immediately after O_2 exposure. Converting the intensity ratio to monolayers of oxygen using Equation (1) gave a value of 0.38 ± 0.04 ML, in excellent agreement with currently accepted values [1, 18]. It is also significant here that a value of 0.35 ± 0.0 4 ML in complete agreement with ours was derived for this value in an independent XPS study by Brundle and Hopster [28] using an empirical O 1s intensity calibration via a saturated monolayer of CO on Ni(001) at liquid nitrogen temperature.

As noted above, the saturated oxide thickness after a 1200 L exposure at ambient temperature was determined from the ratio of the O 1s peak area of the oxide and the Ni $2p_{3/2}$ peak area of the clean surface immediately before oxygen exposure. This procedure was used to avoid the complications of having to allow for the intensity of the chemically-shifted Ni $2p_{3/2}$(oxide) peak [1, 29], as well as the attenuation of the Ni $2p_{3/2}$(metal) peak in passing through an oxide layer of unknown thickness. Using this approach, only the attenuation due to the O 1s signal passing through the oxide layer needs to be considered. In order to illustrate the importance of electron attenuation, if we assume that the oxide overlayer is completely non-attenuating, we get from Equation (1) an oxygen coverage of

2.4 ML with respect to the Ni(001) surface density. (The saturation coverage shown in Figure 4 is slightly higher than this at about 2.8 ML, but these results were obtained at a later stage of the study after a number of ion bombardment and annealing cycles. It was found that the resultant aging of the crystal surface led to somewhat higher oxygen uptake values versus exposure.) This is an absolute minimum according to our XPS analysis, as it neglects overlayer attenuation. On the other hand, if the oxide overlayer attenuates the XPS signal, the more correct Equation (3) gives an oxygen coverage of 4.7 ± 0.5 ML, an increase of nearly a factor of two, thus underscoring the importance of attenuation corrections in coverage measurements. As stated in our earlier paper [13], this saturated oxide thickness is larger than the 2–3 ML that has previously been reported from some studies in the literature [1]. The absolute minimum of 2.4 ML that we find is furthermore inconsistent with the saturation coverage of 2.45 ML found recently by Pope *et al.* using nuclear reaction analysis [18], since the presence of any reasonable attenuation in the oxide overlayer in XPS would yield a higher value than 2.45. Our value of 4.7 ML with overlayer attenuation is however, consistent with, although somewhat higher than, a very recent XPS study of O/Ni(001) by Hall *et al.* [30], who find a 4-ML thickness for the NiO(001) orientation that we find to be dominant at saturation.

3.2. PHOTOELECTRON DIFFRACTION CALCULATIONS-

The single scattering cluster (SSC) model used for the photoelectron diffraction calculations in this study has been discussed in detail elsewhere [19] and we have used it in a form that contains both spherical-wave scattering and the correct s→p final state in O 1s photoemission. The latter two improvements make use of the Rehr-Albers separable Green's function approach [31(a)] which simplifies the calculation of the effective scattering factors. In the case of O 1s emission from a multilayer system such as NiO(001) or

NiO(111), where it is possible to have more than one type of emitter in each layer, it is important to correctly weigh the intensities of each emitting atom in the final intensity sum. The weight used is the number of each type of emitter per unit area in that layer divided by the total number of emitting atoms per unit area present in the layer. Attenuation of the photocurrent from each oxide layer is then provided by a exponential factor of the form $\exp\left(\frac{-z}{2\Lambda_e \sin\theta}\right)$, where z is the depth below the surface. Such weighting considerations are also important in the estimation of the percentage of NiO (one O atom per Ni atom multiplied by the number of monolayers of NiO(001)) mixed in with c(2×2)O ($^1/_2$ O atom per Ni atom), a point that will be discussed in greater detail later.

A more sophisticated program that takes into account photoelectron multiple scattering (MS) events is also available to us, although computer-time constraints limit the size of the clusters that can be used at present to about 30–40 atoms [32, 33]. In general, MS effects in XPD are not significant unless there are long rows of atoms present in the cluster which lie within about 10° of the photoemission direction [32, 33]. MS also may produce some effects for the thicker annealed oxide, where it would be expected to yield a reduction of the intensity of the forward scattered peaks predicted by SSC theory, but it is not expected to significantly influence the conclusions of this analysis.

The input parameters for the SSC program include the following for O 1s emission: For the c(2×2) analysis, clusters of various sizes were investigated and it was found that a cluster having a minimum radius of 20 Å from the emitter is necessary to insure full convergence of all the diffraction features at the lowest takeoff angle of $\theta = 8°$ [see, for instance, Figure 16 in Reference 19(c)] and this was used throughout the analysis for consistency. An inner potential of 11.0 eV was used for the c(2×2) overlayer, along with an inelastic attenuation length in the overlayer of 12.3 Å, although small changes of ~±20% in either value did not significantly change the outcome of the calculated diffraction curves. For the oxide, a number of different clusters having two or more layers of NiO, as well as

having different radii from a minimal five-atom cluster up to a fully converged cluster of 20 Å in radius, were used to investigate the effect that annealing has on the vertical and horizontal order of the oxide layer. For the oxide, the inelastic attenuation length remained unchanged at 12.3 Å, but the inner potential was increased to 13.2 eV, a number obtained from a band structure calculation by Mattheiss [34].

3.3. R-FACTORS FOR COMPARING EXPERIMENT AND THEORY-

The five R-factors (R_1–R_5) used in this study to judge the goodness of fit between experimental azimuthal data and theory are based essentially on the ideas of Van Hove, Tong, and Elconin [35]. However, a significant improvement we have incorporated is in the manner of normalizing the experimental data with the theory. This normalization is motivated by the observation that the theoretical anisotropies as judged by$(I^{max}-I^{min})/I^{max}$ typically exceed those of the experimental results by a factor of between two and three. Such a discrepancy can be attributed to MS effects, surface roughness, finite domain sizes, and other non-ideal surface effects. Our basic strategy is to force the normalized theory curve to have an anisotropy as close as possible to that of experiment before direct comparison. The normalization routine is as follows: The experimental diffraction curve is forced to have an amplitude between zero and one,

$$I^{*}_{exp}(n) = \frac{I_{exp}(n) - I^{min}_{exp}}{I^{max}_{exp} - I^{min}_{exp}} ,$$

where $I^{*}_{exp}(n)$ is the rescaled experimental intensity for the n^{th} channel in the azimuthal scan, $I_{exp}(n)$ is the raw experimental data for the n^{th} channel, and I^{max}_{exp} (I^{min}_{exp}) are the maximum (*minimum*) values of $I_{exp}(n)$ in the azimuthal scan. Next, the average value of both the

rescaled experimental and original theoretical curves is set to zero by subtracting out the average value of the rescaled experimental and the raw theoretical curves:

$$I^{**}_{exp}(n) = I^{*}_{exp}(n) - \frac{1}{n}\left[\sum_{n} I^{*}_{exp}(n)\right]$$

and

$$I^{*}_{th}(n) = I_{th}(n) - \frac{1}{n}\left[\sum_{n} I_{th}(n)\right] .$$

The average value of both the rescaled experiment and theory is given by,

$$\bar{I}^{*}_{exp} = \frac{1}{n}\left[\sum_{n} I^{*}_{exp}(n)\right] \qquad \text{and} \qquad \bar{I}^{*}_{th} = \frac{1}{n}\left[\sum_{n} I_{th}(n)\right] .$$

The rescaled theory, $I^{*}_{th}(n)$, then is forced to have the same $\pm$area relative to the average zero as the rescaled experimental data, $I^{**}_{exp}(n)$. The final scaled theory curve is then $I^{**}_{th}(n)$, as given by:

$$I^{**}_{th}(n) = I^{*}_{th}(n)\left[\frac{A_{exp}}{A_{th}}\right] ,$$

where the $\pm$ areas, A_{exp} and A_{th}, are given by:

$$A_{exp} = \sum_{n}\left|I^{**}_{exp}(n)\right| \qquad A_{th} = \sum_{n}\left|I^{*}_{th}(n)\right| .$$

•In the final step in the normalization, a vertical offset is added to give the normalized theory curve approximately the same maximum value as the original experimental curve. This vertical offset is defined as:

$$\text{offset} = \bar{I}^{*}_{exp} + \frac{I^{min}_{exp}}{I^{max}_{exp} - I^{min}_{exp}} \cdot$$

so that,

$$I^{\ddagger}_{exp}(n) = I^{**}_{exp}(n) + \text{offset}, \quad \text{and} \quad I^{\ddagger}_{th}(n) = I^{**}_{th}(n) + \text{offset}.$$

Because these final normalized intensities are still absolute, with no background subtracted from them, they yield the very desirable property for XPD analyses that two curves with a lower percent effect (or lower overall anisotropy = $(I^{max} - I^{min})/I^{max}$) contribute less to four of the five R-factors defined below. Thus, the contributions of azimuthal scans with different anisotropies to R are automatically weighted correctly in the summed R's to be discussed below.

These normalized intensities are finally substituted into the five R-factors R_N (N = 1, 2, 3, 4, 5) as defined by Van Hove *et al.* [35] to yield:

$$R_1 = \frac{\sum_n \left| I_{exp}(n) - I^{\ddagger}_{th}(n) \right|}{\sum_n \left| I_{exp}(n) \right|}, \qquad (4)$$

$$R_2 = \frac{\sum_n \left[I_{exp}(n) - I_{th}^{\ddagger}(n) \right]^2}{\sum_n [I_{exp}(n)]^2} ,$$

R_3 = percentage of angle range over which $I_{exp}(n)$ and $I_{th}^{\ddagger}(n)$ have slopes of different sign (+/-),

$$R_4 = \frac{\sum_n \left| I'_{exp}(n) - I_{th}^{\ddagger'}(n) \right|}{\sum_n \left| I'_{exp}(n) \right|} ,$$

where $I'_{exp}(n)$ and $I_{th}^{\ddagger'}(n)$ are the first derivatives of the experiment and normalized theory respectively, and lastly,

$$R_5 = \frac{\sum_n \left[I'_{exp}(n) - I_{th}^{\ddagger'}(n) \right]^2}{\sum_n [I'_{exp}(n)]^2} .$$

Finally, for a set of azimuthal diffraction data from a given surface structure, we can calculate "global" or "summed" R-factors for any one of the five choices as:

$$R_N(\text{total}, z) = \frac{1}{m} \sum_m R_N(m, z)) , \qquad (5)$$

where N is the N^{th} R-factor, z is some structural parameter(s) that is being varied, and m is the number of azimuthal scans at different polar angles taken for that surface structure. In a large number of tests, we find that all five R-factors give very similar results (as will be illustrated below for one example) and that they are also consistent with straightforward visual evaluations of fit. These R-factors are also found to be superior for XPD to others that we have tested such as those of Zanazzi and Jona [36]. We have further found that the first R-factor (R_1) provides an excellent description of the fit between curves by itself and it is this value that is reported in most cases throughout this paper.

4. RESULTS AND DISCUSSION:

4.1. SOME STRUCTURAL CONSIDERATIONS-

Figure 4 is a schematic drawing of the two primary structures that we will be concerned with on the Ni(001) surface. By varying the takeoff angle of the O 1s azimuthal scans, it is possible to tune the analysis from sampling preferentially near-surface features at low θ values to probing more bulk-like structural information at high θ values. From Figure 4(a) for c(2×2)O, we see that, in order to obtain structural information on the oxygen-to-nickel interplanar separation or z-distance, rather large scattering angles (θ_{Ni}) are involved, but these can be minimized by using grazing emission directions, thus increasing the scattering that comes from the underlying Ni atoms. The scattering angles for other O atoms (θ_O) are by contrast constant at $\theta_O = \theta$ = takeoff angle. From Figure 4(b) for the oxide, we can also use grazing emission directions to derive structural information more sensitive to the surface plane, or larger polar angles to probe the structure of the oxide buried further beneath the surface. Due to the epitaxial nature of the NiO(001) oxide that

forms on Ni(001), information on both the distance separating the first and second NiO planes (a_{12}) and that separating the second and third planes (a_{23}) is relevant.

4.2. KINETICS OF THE OXYGEN UPTAKE ON Ni(001) AND THE ONSET OF NiO FORMATION-

In order to systematically monitor the dependence of the oxygen coverage on exposure, the O 1s and Ni $2p_{3/2}$(metal) XPS intensities were measured at various sequential oxygen exposures up to 1300 L for a substrate temperature of ~300 K. These intensities were observed along $\theta = 45°$ and $\phi = 13°$, a direction chosen such that it represented an average over the Ni $2p_{3/2}$ diffraction structure in order to minimize the influence of diffraction effects on the final oxygen coverages. The importance of this kind of correction has been discussed for c(2×2)S on Ni(001) by Connelly *et al.* [26(c)]. The intensity ratios were in this figure converted to monolayers coverage using the more approximate Equation (1), which assumes that the oxide layer is completely non-attenuating, and thus leads to too-low oxide coverages that are simply proportional to the O 1s/Ni $2p_{3/2}$ intensity ratios. The results of these measurements and the concomitant LEED patterns are illustrated in Figure 3(a), with a blowup of the critical 10 L–120 L region also presented in Figure 3(b). Also included in the figures are the recent temperature-dependent O/Ni Auger ratio measurements for this system by Wang *et al.* [14] at 300 K (shown as the short dashed curve), 350 K (dashed curve), and 400 K (long dashed curve), all of which have been normalized to have the same magnitude as the XPS curve at an exposure of 30 L which corresponds to the minimum-slope reference point in our c(2×2) "plateau". All four curves display the characteristic two-step uptake curve that is in excellent agreement with the pioneering Auger results of Holloway and Hudson [3].

The length and relative flatness of our coverage curve near 30 L is in best agreement with the Auger results at 350–400 K, and suggest that, during XPS analysis, our specimen may have been heated somewhat above ambient temperature. However, the fact that our curve seems to reach saturation considerably more slowly than the other three also suggests that our surface could have had less surface defects and thus inherently lower reactivity. The dashed Auger ratio curve for 350 K further shows a final saturated oxide value that agrees very well with the results of our kinetics curve, indicating a degree of self-consistency between the XPS and Auger data.

The results of our LEED observations have been described in earlier figures in Reference 13. A very faint c(2×2) pattern was observed at a coverage of 10 L. This replaced a weak p(2×2) pattern that was present at 1 L. This c(2×2) pattern slowly increased in intensity and displayed its strongest and sharpest diffraction spots over the relatively flat c(2×2) plateau region from 30 L to 70 L, after which it slowly turned into rather large and hazy spots before disappearing altogether after a total exposure of 300 L. It is important to note that the final disappearance of the c(2×2) structure occurred well after the first appearance of the NiO LEED patterns at 150 L. The oxygen coverage showed a very rapid increase in the region of 100–300 L that is due to the rapid growth around existing oxide nuclei. At approximately 150 L or 0.85 ML coverage, the individual domains of NiO become sufficiently large to be observable with LEED. Two types of LEED patterns associated with this oxide are seen, a stronger p(1×1) of NiO(001) and a weaker 12-spot ring; the latter is thought to be characteristic of two orientations of NiO(111) rotated 30° apart. At our ambient-temperature exposure conditions, these two LEED patterns slowly increased in intensity with increasing oxygen exposure all the way up to saturation. As mentioned earlier, the last traces of all c(2×2) structure were finally removed at 300 L, but it was not until 800–1200 L that the oxygen uptake nearly ceased, indicating that the oxide had finally saturated the surface.

A careful inspection of the LEED pattern at 1200 L revealed the previously discussed splitting of the large and rather hazy NiO(001) spots into a centered square arrangement [13]. From the position of the NiO(001) spots and their rather diffuse nature, it was suggested by Saiki *et al.* that this is the result of the NiO(001) overlayer having a lattice constant parallel to the surface that is expanded by $^1/_6$ relative to the underlying Ni(001) substrate. This oxide would thus be under considerable strain due to largely incommensurate growth on the underlying Ni(001) mesh. The superposition of (6×6) NiO(001) unit cells on (7×7) Ni(001) unit cells creates a single NiO(001)/Ni(001) superlattice unit cell, which is believed to be the origin of the centered spot splitting that was reported earlier. Wang *et al.* [14] have also subsequently studied the LEED spot profiles and integrated intensities for this system as a function of temperature.

As noted earlier, the presence of small islands of NiO that apparently coexist with the majority c(2×2) species is thought to be the reason that a very early XPD study by our group reported that the oxygen position in the c(2×2) structure is a fourfold hollow site and very close to the in-plane position [1, 5]. For such a structure, the diffraction data would be strongly affected by the forward-scattering effects from even a small amount of oxide present in the near-surface region, especially if the data were taken at grazing emission directions, as illustrated in Figure 4(b). In fact, the exposure used to study c(2×2) in this prior XPD work was 100 L, and the associated oxygen coverage was ~1.0 ML. In the present study, we have both used what appears to be a higher quality and less reactive surface, and chosen significantly lower exposures to minimize such oxide effects. Azimuthal data taken at sufficiently large takeoff angles should, at least in principle, be able to detect the presence of buried oxide islands provided that these islands are at least 2-ML thick and that they display some kind of epitaxial-like growth. Two such emission directions are shown by the arrows in Figure 5(a) for 2-ML of NiO(001) grown on the Ni(001) surface, and they correspond to oxygen forward scattering, which is expected along

the [101] emission direction at $\theta = 45°$ and $\phi = 0°$, and also to nickel forward scattering along the $[1\bar{1}1]$ direction at $\theta = 35°$ and $\phi = 45°$.

In order to search for oxide nuclei effects, a series of O 1s azimuthal scans was taken at various oxygen exposures from 30 L up to the saturated oxide at 1200 L. The curves shown in Figure 6 were taken at $\theta = 36°$, which is very close to passing through the $<1\bar{1}1>$ directions, while those in Figure 7 were taken at $\theta = 46°$, close to the <101> directions. Here, the experimental data are shown as the solid curves and they were compared with the results of different SSC calculations, which appear as dashed curves. The experimental data at 30 L represents the diffraction pattern for the best c(2×2) overlayer ($\Theta \approx 0.4$ ML), 70 L should include some oxide nucleation ($\Theta \approx 0.5$ ML), 150 L is the point where LEED first detects the presence of NiO ($\Theta \approx 0.8$ ML), and of course, 1200 L represents the saturated oxide. Theoretical calculations were done for a c(2×2) overlayer with the oxygen sitting in the fourfold hollow sites at the generally agreed upon height of z = 0.75 Å and for a saturated oxide made up of 2-ML of NiO(001), but with various cluster sizes to mimic the effect of small domains and/or strain. These oxide clusters include a minimal five-atom cluster having only short range order [dark-circled atoms in Figure 5(b)], an intermediate-sized 35-atom cluster covering about two unit cells [Figure 5(b)] whose a_{12}-spacing has been expanded by 0.2 Å in an attempt to approximate the expected effect of relaxation in the vertical direction in response to the ~1.4% compression in both lateral directions, and by a much larger, fully converged cluster of ~20 Å in radius, containing approximately 200 atoms. Also shown is the calculated result for a fully converged 2-ML thick NiO(111) cluster, including a summation over two equally populated domains rotated by 30° with respect to one another. The theoretical curves make it clear that XPD is primarily sensitive to short range order, as calculations for both the minimal five-atom cluster and the intermediate 35-atom cluster contain all of the major diffraction features present in the much larger and fully converged 20 Å cluster.

The experimental diffraction pattern of the saturated oxide in Figure 6 clearly shows the effect of strong O-to-Ni forward scattering at $\phi = 45°$, and the shape of the curve remains essentially unchanged until ~70 L where approximately 0.5 ML of oxygen is present. The experimental anisotropy has dropped from a high of 28%, down to only approximately 7% over this exposure range, and there is a corresponding increase in the statistical uncertainty due to a reduction in the O 1s integrated intensity as the exposure is reduced. A similar effect is observed for the primary diffraction features in Figure 7 at $\theta = 46°$. The primary peaks are centered at $\phi = 0°$ and 90° and are due to the slightly less intense O-to-O forward scattering. Qualitatively, the observed oxide diffraction patterns are not at all consistent with those expected from NiO in the (111)-orientation; by contrast, they are in rather close agreement with the predicted patterns for NiO in the (001)-orientation, especially for the minimal five-atom cluster and for the intermediate 35-atom cluster with the 0.2 Å vertical expansion.

Turning now to the c(2×2) overlayer at 30 L, we see that a comparison of the experimental data at 30 L with fourfold c(2×2) theory at $z = 0.75$ Å agrees reasonably well with the positions of some of the major diffraction peaks, even though such features are very weak, with experimental anisotropies in the 5–9% range and theoretical anisotropies of 20–4%, respectively. However, certain features in the experimentally-derived curves at 30 L appear to represent forward scattering effects due to a small amount of oxide or buried oxygen in the subsurface region. This conclusion is based on a filling-in of the central valley with a weak peak at $\phi = 45°$ in Figure 6, and the much clearer oxide-like forward scattering peaks at $\phi = 0°$, 90° seen in Figure 7. These forward scattering peaks in Figure 7 are quite intense and they persist down to 30 L, with a significant anisotropy of 8.6%, where they greatly exceed the anisotropy predicted for the c(2×2)O structure. These peaks thus clearly indicate the presence of buried oxygen emitters, probably in the form of small nuclei of NiO(001) mixed in with the c(2×2) overlayer. An R-factor analysis of the experimental

data at 30 L and $\theta = 46°$ (Figure 7) with theoretical curves generated by a simple mixing of the c(2×2) structure with various percentages of 2-ML of NiO(001) resulted in the conclusion that about 10–15% of the oxygen atoms are present in such buried sites. These results are consistent with a recent STM study of this system by Wilhelm *et al.*, who see evidence for oxide island formation at as low as 10 L O_2 exposure [16].

Such high-takeoff-angle XPD data is thus seen to be extremely sensitive to minority species that are somehow in subsurface sites, a generally useful characteristic for future studies of oxidation and epitaxy.

4.3. STRUCTURE OF NiO(001) ON Ni(001)-

In discussing our data for the saturated oxide, we will first consider O 1s polar scans, and then O 1s azimuthal scans. Figures 8(a) and 8(b) present O 1s polar scans for both the unannealed and annealed oxide at 1200 L exposure (solid curves), as taken along the <101>- and <1$\bar{1}$1>- azimuths respectively. The accuracy of the shapes and positions of these curves was confirmed by comparing scans obtained along the four symmetry-equivalent azimuths 90° apart. These experimental data are also compared in these figures to several SS calculations (dashed curves) derived from a variety of clusters. The primary diffraction feature observed along the <101> azimuth for the unannealed surface is a strong peak centered at $\theta = 47.8°$ which shifts to a lower angle of $\theta = 46.6°$ on annealing. There are two other minor features, a weak peak at $\theta \approx 39°$ for the unannealed case which appears as a shoulder in the annealed curve, and a weak shoulder at $\theta \approx 54°$ that is more evident in the unannealed case. Along the <1$\bar{1}$1> azimuth, the unannealed curve shows a single broad peak centered near $\theta \approx 37°$–$38°$, which on annealing sharpens slightly to form the primary peak centered near $\theta \approx 39°$; in addition, the annealed data shows weak additional features at $\theta = 28°$ and $\theta = 49°$.

While simple forward scattering arguments can be used to determine the approximate positions of all of the major diffraction features, the actual peak positions are pushed upward by several degrees from the ideal <101>- and <1$\bar{1}$1>-emission directions at $\theta = 45°$ and $\theta = 35.3°$ respectively. These shifts are furthermore opposite in direction from those expected due to electron refraction by the substrate inner potential (V_o). In this study, a value of 13.2 eV was used as the inner potential for the oxide surface in the SSC calculations [34], and this results in a downward shift of the external electron trajectories by about 0.5° at the polar angles examined. Thus, the observed upward shifts appear to be due to real structural effects.

Assuming for the moment that the oxide overlayer contains at least 2-ML of NiO(001) (we will later with our azimuthal data confirm that NiO(111) is a minority species under our conditions of exposure), the forward scattering peak along the <101>-direction would correspond to O-Ni scattering while the peak in the <1$\bar{1}$1>-direction would be due to O-O scattering, as indicated in Figure 5. It should then in principle be possible to determine whether there is any relative vertical relaxation of the O and Ni surface atoms within the surface plane from the corresponding shifts in the position of the forward scattering peak from the ideal polar angles of 45.0° and 35.3°. As described in a prior XPD/LEED paper on this system by Saiki *et al.* [13], the two-dimensional lattice constant in the surface plane was deduced from LEED measurements and it was concluded that the oxide was expanded by $^1/_6$ or 16.7% over $a_{Ni} = 3.52$ Å, and that this expansion to $a_{NiO} = 4.11$ Å remained essentially unchanged on annealing the oxidized surface. Since the lattice constant of bulk NiO is 1.184 times that of Ni, or 4.17 Å, there is a residual lateral compression of 1.4% in this model. The 1.2° shift of the primary diffraction peak along the <101>-direction to higher polar angle between the unannealed and annealed data thus could be due to a simple expansion of the unannealed oxide lattice in the vertical direction so as to reduce the strain imposed by being compressed laterally by the underlying Ni(001) mesh. Such a shift in the

θ-angle of 1° to 3° corresponds to a vertical expansion of between 0.1 Å to 0.3 Å, a reasonable amount if the NiO(001) unit cell is actually trying to conserve its volume when compared to bulk NiO. In fact, in conserving volume relative to bulk NiO, the required expansion leads to a vertical unit cell height of 4.30 Å = $a_{12} + a_{23}$, or a 0.2 Å overall vertical expansion relative to the lateral a_{NiO}. In the unannealed data, a similar shift along the <1$\bar{1}$))1>-direction was not so clearly observed; however, the rather broad peak featured in this data could easily hide such a shift. The annealed data for <1$\bar{1}$1> shows as much as a 4° shift. These results could imply that only the oxygen in the surface plane of the unannealed oxide has been displaced upward by ≈ 0.2 Å, as suggested previously [13], but in the present analysis, we have expanded our search to include various increases in the a_{12} spacing (thus moving both O and Ni atoms upward equally), as discussed further below. Taking the <101> or <1$\bar{1}$1> data together, Figure 8 shows that the best fit for the polar unannealed data is finally found for an intermediate-sized 35-atom cluster where just the oxygen atoms are moved upward by 0.2 Å.

An attempt to model the annealed oxide was done using much larger and fully converged clusters of 20 Å in radius and with 2-, 3-, and 4-ML thicknesses. While the $a_{//}$-spacing was fixed at the value of a_{NiO} = 4.11 Å derived from our LEED results, the a_{12}-spacings in the perpendicular direction were allowed to vary. Two interesting observations were made. First, for those clusters having no vertical expansions and designated as being "cubic", the centers of the diffraction peaks along the <101>-direction were shifted downward by 0.5° to θ = 44.5°, as expected from simple electron refraction due to the surface inner potential. In order to explain the significant observed shift in the opposite direction, something more is clearly needed. As shown in Figure 8(a) for the 2-ML, 20 Å cluster that had a_{12} increased by 0.2 Å, this expansion is sufficient to shift the emission direction to the higher polar angles required. The second observation is that, along the

<$1\bar{1}1$>-direction, the most intense diffraction feature in both experiment and theory occurs at $\theta \approx 39°$–$40°$ and is thus not simply relatable to the O-Ni forward scattering direction at $\theta = 35.3°$. Probably this peak has contributions from higher order interferences whose position is sensitive to both the expansion in the vertical direction and to the thickness of the oxide film. The best fit for the annealed data in this azimuth is found to be for a 2- or 3-ML cluster having either little or no expansion of the vertical interplanar spacing, but the evidently more complex nature of the interference effects involved with this direction make this conclusion less reliable.

A rigorous analysis of the polar data using R-factors was not possible due to the presence of a non-linear background that is caused by a difficult-to-measure instrumental response function for a multilayer thin film [19, 24]. This response function is expected to behave roughly as $\sin\theta$. Data obtained by fixing the polar angle and scanning over azimuthal angles do not exhibit such response function effects, and we consider these now.

Low angular resolution O 1s azimuthal data were taken for the unannealed oxide over the range of $\theta = 43°$ to $47°$ in $1°$ steps, although only the results at $\theta = 43°$, $45°$, and $47°$ are shown in Figure 9. The experimental data (shown as the solid curves) were taken over the full $360°$ azimuthal range and fourfold averaged to improve the statistical reliability before being plotted over one quadrant from $\phi = 0°$ to $90°$. The primary diffraction features are the peaks centered at $\phi = 0°$ and $90°$; these correspond to the strong forward scattering that is expected along <101> emission directions (see, for example, Figure 5). These strong diffraction peaks also exhibit shoulders located approximately $14°$ to either side of their centers; these shoulders gradually decreases in significance as the polar angle is increased from $\theta = 43°$ to $\theta = 47°$. There is also a very strong diffraction feature centered at $\phi = 45°$ and it too, decreases in relative intensity as the polar angle is increased. As discussed in the prior XPD analysis of this system [13], this peak appears as a doublet in the annealed oxide data (as will be discussed further below), but appears as a singlet in the unannealed data,

providing a clear indication of the structural differences between the unannealed and annealed forms of the oxide. One contribution to the peak at $\phi = 45°$ is first-order interference [19] associated with forward scattering along <101> directions, although other forward scattering processes along higher-order directions also may contribute, as first pointed out for XPD from epitaxial Cu(001) films by Bullock and Fadley [37]. The anisotropy varies between 20–22% over the entire unannealed data set from $\theta = 43°$ to 47°; this is quite low when compared to the annealed data to be discussed later, which yield 35–53%. These anisotropy results suggest less long-range order and/or smaller domain sizes of the individual NiO islands in the unannealed case.

These observations prompted our use of smaller clusters to simulate the loss of long-range order for the unannealed data . In Figure 9, we compare experiment to calculation for several different clusters: a 35-atom cluster such as that shown in Figure 5(b) in which $a_{\perp}$ and $a_{//}$ are equal ("no expansion" or "cubic"), the same cluster with the top-layer O atoms moved up by 0.2 Å, and the same cluster with a_{12} increased by 0.2 Å (so that both O and Ni atoms are moved up). Also shown are theory curves for the minimal five-atom cluster in Figure 5(b). A visual comparison of experiment and theory readily indicates that the larger cluster with oxygen , and perhaps also nickel, displaced upward by ~0.2 Å best describes the data, although the agreement is not as good for $\theta = 47°$ as for the two lower angles.

Continuing with the analysis of the unannealed data, we note that the intermediate-size 35-atom cluster covers an area of approximately 5 Å in radius or approximately two unit cells of NiO and yields results that are very similar in appearance to those of much larger 20 Å clusters that were used in a prior analysis of annealed XPD azimuthal data [13]. In order to better quantitate our analysis of this data, we have carried out an R-factor analysis as summed over all of the azimuthal data using Equations (4) and (5), and these results for various a_{12}-expansions are summarized in Figure 10. The filled circles and solid

curve represent 2-ML thick, 35-atom clusters whose a_{12}-distance has been expanded in 0.1 Å steps from the reference value of the $a_{//}$-spacing that is fixed at 4.11 Å. The best fit is found for an expansion of a_{12} between 0.1 Å and 0.2 Å, and it is better than what is obtained by simply moving the oxygen atoms in the surface plane upward by 0.2 Å (upward pointing triangle), or by going to the minimum five-atom cluster (downward pointing triangle), with the latter two structures displaying about equally good fits. This expanded structure is consistent with the results of the earlier polar analysis that suggested a small expansion of the a_{12}-spacing is needed to match the tilt to higher polar angles of the principle forward scattering features.

Comparing experiment with theory at the optimal a_{12}-expansion of 0.2 Å in Figure 9, shows excellent agreement at the lower end of the θ-range. At $\theta = 43°$, the positions of all of the features are well very reproduced, with the only minor discrepancy being the relative peak height of the forward scattered peak at $\phi = 0°$ and 90°. At $\theta = 45°$, the primary discrepancy is that theory predicts too broad a feature at $\phi = 45°$, a problem which becomes worse on going up to $\theta = 47°$. The forward scattering peaks and their shoulders are a little too well-resolved compared to the experiment and this may indicate that a smaller cluster (i.e., less long-range order) would be useful and/or that a greater amount of surface disorder and strain may be present than is possible to take into account in the calculations.

To conclude this discussion of the unannealed oxide data, we find evidence in both polar and azimuthal data for vertical displacements in the top layer by approximately 0.2 Å, although the closeness of the R-factors for the several structures explored does not permit ruling out some mixture of structures with O, as well as Ni, shifted upward, and with less long-range order than our 35-atom cluster possesses. In fact, the (6×6) NiO/(7×7) Ni superlattice that has been proposed previously [13] would be expected to lead to regions of more order/less strain and less order/higher strain over the superlattice unit cell. Thus, the XPD measurements will certainly be averaging over a number of local environments, and the

best we can hope to do from this kind of analysis is to estimate the average or most typical type of structure.

We now consider analogous azimuthal data for the annealed oxide over the $\theta = 43°$-47° range, but with the important difference that the angular resolution is now significantly better at ±1.5°. These experimental data also were taken in θ steps of 1°, with the entire set being shown in Figure 11. The anisotropies of the experimental curves vary from a low of 36% up to a very high value of 53%, and there is much more fine structure than in the unannealed data of Figure 9. These curves posses a remarkable sensitivity to small changes in θ that has also been seen in the high-resolution work by Osterwalder *et al.* [38] on Ni $2p_{3/2}$ substrate emission from clean Ni(001).

Figure 11 shows that the primary diffraction features common to this set of curves are the strong forward scattering peaks that appear along the <101>-equivalent directions at $\phi = 0°$ and 90° (as seen also in Figure 9). The central region at $\phi = 45°$ exhibits a wide, mesa-like peak at $\theta = 43°$. This peak splits into a doublet as the emission angle is raised above $\theta = 44°$, and this doublet is best resolved at $\theta = 45°$. Other experimental diffraction features include a somewhat weaker peak that is strongest for $\theta = 43°$ and centered at ϕ = 10°–22°; this peak continuously decreases in height as the polar angle is increased, essentially disappearing at $\theta = 47°$. Finally, a small shoulder is observed at $\theta = 43°$ and ϕ = 23°, and this gradually increases in size until it is a well-defined although rather weak peak at $\theta = 47°$. It is thus clear from Figure 11 that the richness of the diffraction fine structure can be used to clearly differentiate curves separated by only 1° in polar angle!

These high-angular-resolution annealed azimuthal data were also analyzed by comparing them to theory with the summed R-factor (R_1) discussed earlier. SSC calculations for a cluster of 20 Å in radius containing approximately 120 atoms per layer were done to determine the best structural fit, and such large clusters were found to be necessary to predict of all the diffraction features present . Based on a preliminary XPD

analysis of this system [13] which showed that the best visual fit for the annealed oxide was with 2-ML of NiO(001), a number of calculations were done to both check this and to see whether clusters having an expanded $a_{\perp}$ lattice constant might better describe the data. In Figure 12, several theory curves are compared to experiment for $\theta = 43°$, 45°, and 47°, and in Figure 13, the summed R_1 results for a variety of structures are shown. The curves for 2-, 3-, and 4-ML of cubic oxide (no vertical expansion) all predict the locations and relative intensities of the experimental diffraction features very well, with the summed R_1 results in Figure 13 (shown as the open circles connected by the line) yielding a better fit for 3-ML of oxide. The prior XPD analysis [13] only looked at the azimuthal results at $\theta = 35°$ and 45°, with both polar angles including emission directly along low index directions, and so was not as sensitive as the present data set to minor differences with thickness.

The structural parameters for the annealed oxide were also further adjusted by allowing various expansions in both the a_{12}- and a_{23}-spacings. An expansion of the 2-ML NiO(001) model so as to increase a_{12} by 0.1 Å (shown in Figure 13 as the solid circle) results in a significantly higher R-factor, and other larger expansions are off scale and give rise to noticeably poorer fits. After a number of trials, we determined that the best summed R_1 fit was for a cluster having an unequal $a_{\perp}$-expansion; that is, the a_{12} distance was found to be increased by 0.1 Å , with no expansion in the a_{23} separation over the reference cubic structure where $a_{\perp} = a_{//} = 4.11$ Å (point denoted by a filled diamond). For this structure, the comparison between experiment and theory shown in Figure 12 is excellent throughout the lower θ-range, with some minor discrepancies in the mid-ϕ range arising by the maximum $\theta = 47°$.

For the annealed oxide data, the polar and azimuthal results are again consistent, both indicating 2–3 ML of highly ordered oxide with domains at least 20 Å in radius and an a_{12} expansion by about 0.1–0.2 Å. Beyond this, we note that our XPS intensity analysis of the unannealed oxide indicates a total of 4–5 ML of oxide, whereas the XPD results are best

fit for 2–3 ML. Thus, if we assume the total thickness of the annealed oxide to be at least 4–5 ML thick also, the bottom 1–2 layers of it may be much more strained, with stacking faults and defects that could wash out diffraction features.

We turn now to low-θ (grazing-emission) azimuthal data for the unannealed oxide to see what further they can tell us about the structures involved. The contrast between the diffraction patterns of c(2×2)O and of the unannealed oxide are readily apparent in a series of O 1s azimuthal scans taken at θ = 8°, 11°, 14°, and 17°, as shown by the solid curves in Figures 14 and 15. These experimental data were taken for the onset of the sharpest c(2×2) LEED spots (30 L) and for the fully saturated oxide (1200 L). The anisotropies remained fairly constant over this angle range, varying between 19% and 22% for c(2×2) and between 17% and 21% for the unannealed oxide. The experimental oxide curves were compared to single-scattering cluster calculations for two layers of NiO(001) having an intermediate-sized cluster of 35-atoms with an expansion of a_{12} + 0.2 Å and for a cubic cluster about 10 Å in radius, with the former being the structure determined from the analysis of the data at higher θ values. The data for the c(2×2) structure at 30 L is compared with calculations for a c(2×2) overlayer occupying the fourfold hollow site at a *z*-value of 0.75 Å. (This will be seen below as our final structure from this study, in excellent agreement with other recent experimental and theoretical work [15]).

The experiment/theory comparison for the oxide in Figure 14 at θ = 8° and 11° is very good to excellent, with all of the peak positions and most of the relative intensities very well described for either cluster. In Figure 15 at θ = 14°, theory predicts too small a peak along φ = 0° and 90°, and also incorrectly predicts the central peak at φ = 45° to be a doublet. At θ = 17°, theory once again describes the experiment very well, especially the doublet centered at φ = 45°, but while the 35-atom cluster fails to predict a major peak centered at φ = 0° and 90°, this feature is very well described using the slightly larger 10 Å cluster. The difference could be due to a larger effective scattering region for the

photoelectrons along the surface due to the lower takeoff angles involved here. Thus, these data may be sensitive to scatterers further out along the chains of O and Ni scatterers than expected. As one reason for the observed inadequacy of the 35-atom cluster of Figure 5(b) in describing such low-θ emission, it possesses only a single forward scattering atom along the $\phi = 0°$ and 90°, which is insufficient to provide the additional intensity to form the required diffraction peak along this direction for the experimental data at $\theta = 14°$ and 17°.

We have also analyzed these low-θ unannealed oxide data via R-factors for different structures (see Figure 16) and we find that SSC calculations using the larger 2-ML, 20 Å-radius clusters yield summed R_I's (shown as the open diamonds) that are lower than those from the 35-atom cluster (open squares). This analysis clearly rules out the minimal five-atom cluster (downward pointing triangle) and it also leads to the conclusion that a modest increase in the cluster size to 10 Å (shaded circles) gives a somewhat better fit for all vertical expansion values. The optimal structure is a 2-ML,10 Å cluster, with no expansion in the a_{12}-spacing. This lack of an a_{12} increase for these grazing-emission data is thus at first sight in disagreement with the analysis of the polar- and azimuthal-data for higher takeoff angles considered previously. This difference between the low- and high-angle data is not however very large, and it may be due to an effectively longer range along the surface that is seem for grazing emission. High takeoff angles should be more sensitive to the local environment around an oxygen emitter, and we thus believe that these data overall provide evidence for an expansion in a_{12}, even if this is not evident in Figure 16.

It is also worth noting in concluding our discussion of the annealed oxide that our annealing temperature of approximately 523 K is, according to a recent XPS study by Hall *et al.* [30], probably not high enough to produce significant oxide layer thickening that can, for temperatures of 100 K or more above this, lead to oxide islands of as much as 50 Å in thickness.

4.4. STRUCTURE OF c(2×2)O ON Ni(001)-

A series of four O 1s azimuthal scans were performed at 30 L oxygen exposure and for the polar angles of 8°, 11°, 14° and 17°, as shown already in Figures 14 and 15. As mentioned earlier, even at this low oxygen exposure, we estimate that between 10 and 15% of the O atoms are in the form of small oxide islands. We expect such oxide/subsurface species to be more important for higher θ values due to the enhanced electron emission from deeper layers and/or the influence of subsurface oxygen that is responsible for certain forward scattering peaks. We have thus tried to estimate the relative contributions of c(2×2)O and oxide nuclei of 2-ML and 3-ML thickness, as normalized to unit surface area. If we neglect the effect of diffraction on the XPS intensities, the intensity ratios (O 1s, c(2×2)O)/(O 1s, 2-ML NiO) per unit area are 1.1 at θ = 8°, 1.4 at 11°, 1.6 at 14°, and 1.8 at 17°. The corresponding numbers for 3-ML of NiO are 1.2, 1.6, 1.9, and 2.2, respectively. Therefore, in order to minimize the effect of this oxide interference, we have carried out our c(2×2) structural analysis only for the lowest two grazing angles of θ = 8° and 11°. The R-factor analysis of these low-θ azimuthal data was done for a wide range of *z*-distances, but only the region between 0.60 Å and 0.90 Å is shown in Figure 17(a). These SSC calculations used a large clusters of 20 Å in radius to insure full convergence of all the diffraction features, and they were done for the oxygen residing in both the fourfold hollow sites (shown as the solid curve) and in various pseudobridge sites having offsets of 0.1 Å (long dash curve), 0.3 Å (short dash curve) and 0.5 Å (dot-dash curve). The R_1 result for the pseudobridge structure reported by Demuth *et al.* [10], is indicated by the filled circle.

In Figure 17(b), we also address the question of whether the five R-factors considered previously yield similar structural conclusions. For adsorption in the fourfold-hollow site, we here show curves for summed R_1, R_2, R_3, R_4, and R_5 as a function of *z*. It is most encouraging that all of R_1, R_2, R_4, and R_5 yield the same *z* value to within about ±0.02

Å. R_3, which is less analytical in being just a percentage of the interval over which the slopes disagree, shows less regular behavior, and the largest shift in position from the R_1 reference, although even here, the difference in optimum z is only 0.04 Å. We have made similar checks for other cases, and have concluded that the use of R_1 only is sufficiently accurate.

Overall, the best fit to the XPD data is thus found to be for the fourfold hollow site at $z = 0.75$ Å $\pm$ 0.05 Å, which is slightly better than for the best pseudobridge site at $z =$ 0.74 Å and a very small offset of 0.1 Å, and is considerably better than the previously proposed pseudobridge structure with its uncertainty. Note that the pseudobridge site requires four separate domains, each offset along the <110>-equivalent directions, so the average emitter position is in this sense not much different from that for emission from the fourfold hollow site. Curves derived for our optimum fourfold site are compared to experiment in Figures 14 and 15. Agreement is excellent for the two lowest θ values, but not as good for $\theta = 14°$ and $\theta = 17°$, probably due to interference from oxide or buried oxygen. Our final z value, while somewhat lower than some of those previously reported [1], is in excellent agreement with the most recent multilayer LEED and theoretical calculations [15] of this system. We summarize some of the prior structural parameters derived for this system in Table 1; included here are results from low energy electron diffraction (LEED) [15], total energy calculations [15], angle-resolved photoemission fine structure (ARPEFS) [6], surface extended x-ray adsorption fine structure (SEXAFS) [12], and ion scattering spectroscopy (ISS)[11].

Figure 18 compares experiment (solid curve) with theory for the optimum fourfold hollow geometry (long dash curve) and the pseudobridge site of Demuth *et al.* (short dash curve) [10]. The visual agreement is excellent for either structure at $\theta = 8°$, with all of the major diffraction features and relative intensities being very well described, but the fourfold hollow is definitely better at $\theta = 11°$. At $\theta = 8°$, the fourfold hollow curve seems to better

describe the depth of the valley at $\phi = 45°$ and the relative intensity of the doublet centered there, but does a poorer job at determining the relative height of the weak doublet centered at $\phi = 0°$ and 90°. This relatively minor misfit at this polar angle gives the pseudobridge site a marginally better R1 value (0.024 versus 0.030). At $\theta = 11°$, the fourfold hollow site does a significantly better job in predicting the relative intensities of the doublet centered between $\phi = 15°$ and 30° and its mirror equivalent between $\phi = 60°$ and 75°. In particular, the peaks at $\phi = 28°$ and 62° are much better predicted and this is reflected in the much lower R_1 value for fourfold (0.011 verses 0.024 for the pseudobridge site).

As a final general aspect of using such low-θ data to determine the surface structures, we note a potentially confusing type of behavior that has been observed in the R-factors of individual azimuthal scans as the structural parameter z is systematically varied. The tendency is to have a minimum R-factor near the optimum z-distance and then to have periodic local minima at somewhat higher z's, as illustrated in Figures 19(a) and 19(c) for fourfold comparisons to experiment at $\theta = 8°$ and 11°, respectively. The most likely explanation for this quasi-periodicity is pathlength-related variations of the phase between the direct photoelectron wave and its components scattered off the dominant nearest-neighbor Ni scatterers. A schematic of a general scattering geometry is shown in Figure 20. These phase changes of the scattered wave are due to both changes in the geometric path length difference and the scattering phase shift, with the equation describing the locations of successive orders n of constructive interference being:

$$n\lambda_e = r_j(1 - \cos\theta_j) + \frac{\lambda_e}{2\pi}[\psi_j(\theta_j)] \ , \qquad (6)$$

where r_j = the distance to the j^{th} scatterer = $\sqrt{z^2 + d^2}$, θ_j = the associated scattering angle = $\theta + \gamma = \theta + \tan^{-1}(z/d)$, $\psi_j(\theta_j)$ = the scattering phase shift, and λ_e = the electron De Broglie wavelength. Using $\psi_j(\theta_j)$ values from a plane-wave calculation, a nearest-neighbor Ni

distance of $d = 1.762$ Å, $\lambda_e(954\text{ eV}) = 0.40$ Å, and an electron emission angle of $\theta = 8°$, we find that $z = 0.65$ Å for n = 1. Other minima are calculated to be at $z = 1.20$ Å for n = 2 and at $z = 1.66$ Å for n = 3 before passing beyond the z-range of the available R-factor data. In the same way, z values up to n = 4 have been calculated for $\theta = 11°$. These values are indicated in both Figures 19(a) and 19(c) as vertical arrows, and they provide a good estimate of the rate at which the overall phase of the waves scattered from the nearest-neighbor Ni atoms changes by 2π. The fact that the minima in R-factors calculated between experiment and a large-cluster calculation have essentially the same distances between them for both cases is strong evidence for our explanation of this periodicity.

To further test our hypothesis concerning the origin of these oscillations in R-factors, we have performed additional two-atom cluster calculations. In Figures 19(b) and 19(d), two-atom SS calculations involving only one oxygen emitter and one nearest-neighbor nickel scatterer have been compared using the R_1 criterion. Based on the observation that the minimum in R_1 occurs in the experiment/theory for $z = 0.80$ Å at $\theta = 8°$, and for $z = 0.70$ Å at $\theta = 11°$, we have used these same two theory curves as references for comparison in the R-factor analysis; thus we have a two-atom theory-to-two-atom theory comparison resulting in an $R_1 = 0.00$ at these two z-distances. Any effects due to the scattering phase shift will thus automatically be included here. It is striking that we find in these two-atom calculations a series of local minima that exactly matches the periodicity observed in the analysis of the experimental data shown in Figures 19(a) and 19(c).

Summarizing this analysis, the primary contributor in producing these R-factor oscillations with z is the nearest-neighbor Ni scatterer and we have have been able predict the position of the local minima to with a few tenths of an angstrom using Equation (6). Although such oscillations are well known in LEED R-factor optimizations [39], this is the first time to our knowledge that they have been seen in XPD. Such oscillations are expected to be general effects in the analysis of such low-θ data from adsorbates, and considerable

care should be exercised to be sure that a local minimum is not mistaken for the true minimum.

5. CONCLUDING REMARKS:

The interaction of oxygen with Ni(001) is quite complex and it fully deserves the extensive effort put forward to date in an attempt to identify the geometric structures of the various species that grow on this surface. In this study, XPD and LEED have been shown to be a powerful combination of techniques for monitoring the growth of these various surface species from submonolayer adsorption to the saturated oxide. All exposures were done at at ambient temperatures. From our data, we find that the c(2×2)O structure is optimal at approximately 30 L and 0.38 ML coverage. LEED measurements indicate that this c(2×2)O pattern displays its sharpest and most intense spots for oxygen exposures between 30 and 70 L. At higher oxygen exposures, NiO island formation is first observed in LEED for a 150 L exposure and 0.85 ML coverage, with two orientations of the oxide being observed; these are the minority NiO(111) and the majority NiO(001). This oxide diffraction pattern is quite apparent well before the final disappearance of the c(2×2) spot pattern at 300 L. Saturation of the Ni(001) surface in this study was somewhat arbitrarily set at 1200 L, a point at which a significantly larger oxygen exposures did not appreciably increase the oxygen coverage. XPS intensities with proper allowance for inelastic attenuation in the overlayer yield a saturation cover of 4–5 ML of NiO that is larger than that derived in some prior studies; however, only 2–4 ML of this overlayer are found to be sufficiently ordered to lead to the well defined XPD patterns observed.

Using combined polar- and azimuthal-XPD data, we furthermore find clear evidence that oxygen burial and/or oxide nucleation occur well before the end of the c(2×2) "plateau". The presence of such subsurface oxygen is a likely factor in earlier reports of an

in-plane phase for the c(2×2) structure that were done at higher coverages near 0.5 ML. Later studies done at coverages near 0.35–0.40 ML can also be affected by oxide nuclei if the technique is particularly sensitive to subsurface oxygen and no precautions have been undertaken to minimize the interference between the two types of oxygen.

The unannealed saturated oxide grown at ambient temperature forms a superlattice structure that is expanded in the parallel direction by very nearly $^1/_6$ relative to Ni(001), as based on the dimensions of the LEED spot splitting that has been discussed in a prior paper by Saiki *et al.* [13]. A series of XPD data, some taken at a high angular resolution of ±1.5°, show a very strained unannealed NiO(001) overlayer of approximately 2–3 ML in thickness having a lattice parameter (a_{12}) in the vertical direction that is expanded by about 0.2 Å. The size of the individual domains are rather small, averaging between 5 Å and 10 Å in radius. Annealing the surface very briefly to 523 K results in a noticeable increase in order in both the vertical and horizontal directions. Annealing is further found to increase the average thickness of the ordered oxide to between 2- and 4-ML, and the higher angular resolution data permits estimating relative vertical interplanar spacings. We find the a_{23}-spacing to have no expansion, while the two layers closest to the surface, as given by the a_{12}-spacing, have a slight expansion of 0.1 Å.

We have also determined the structure of the c(2×2) overlayer. Grazing emission angles were used to enhance surface sensitivity. Nonetheless, there will be some interference of the O signal from buried NiO due to the presence of in-plane chemisorption sites in oxide nuclei distributed over the more widely dispersed c(2×2) geometry. Comparing theoretical calculations of mixed c(2×2)O and vertically-expanded NiO with experiment yields an estimated 10–15% contribution of NiO to the c(2×2)O intensity at the optimal exposure of 30 L. By further restricting the azimuthal data analyzed to only the lowest two θ values of 8° and 11°, we further suppress this interference due to subsurface oxygen and we finally find the optimal geometry to be for oxygen residing in the fourfold

hollow sites at a z-distance of 0.75 Å. The R-factor for this structure is lower than that for a previously proposed pseudobridge site.

More generally, the results presented here illustrate the utility of XPD, together with single scattering calculations and simple R-factor analysis, for determining structures present in an epitaxial-like overlayer that contains significant amounts of strain due to a misfit of the lattice parameters in the lateral directions. With the development of higher intensity x-ray sources such as those using synchrotron radiation, the routine use of higher-angular resolution studies should permit the study of even deeper lying structures, for example, for buried interfaces, clusters or islands on the surface.

ACKNOWLEDGEMENTS:

This work has been supported by National Science Foundation under Grants CHE 80-21355 and CHE83-20200, and by the Office of Naval Research under Contracts N00014-87-K-0512 and N00014-90-5-1457. One of us (C.S.F.) also gratefully acknowledges the support of the Department of Energy under Contract No. DE-ACO3-76SF00098.

REFERENCES:

† Present address: Lawrence Berkeley Laboratory, Berkeley, CA 94720 USA

‡ Present address: NSLS, Brookhaven National Laboratory, Upton, NY 11973 USA

* Present address: University of Fribourg, CH-1700 Fribourg, Switzerland

†† Present address: National Renewable Energy Laboratory, 1617 Cole Blvd. Golden, CO 80401 USA

** Present address: Univ. of California-Davis, Davis, CA 95616 USA

[1]. C.R. Brundle and J.Q. Broughton, in *The Chemical Physics of Solid Surfaces and Heterogeneous Catalysis*, edited by D.A. King and D.P. Woodruff (North-Holland, Amsterdam, 1991), Vol. 3a. A comprehensive review of the interaction of oxygen on Ni(001) as well as several other single-crystal surfaces can be found here.

[2]. J.E. Demuth, P.M. Marcus and D.W. Jepsen, Phys. Rev. Lett. **31**, 540 (1973).

[3]. P.H. Holloway and J.B. Hudson, Surf. Sci. **43**, 123 (1974).

[4]. D.F. Mitchell, P.B. Sewell, and M. Cohen, Surf. Sci., **61**, 355 (1976).

[5]. L.G. Petersson, S. Kono, N.F.T. Hall, S. Goldberg, J.T. Lloyd, C.S. Fadley and J.B. Pendry, Mater. Sci. Eng. **42**, 111 (1980).

[6]. D.H. Rosenblatt, J.G. Tobin, M.G. Mason, R.F. Davis, S.D. Kevan, and D.A. Shirley, Phys. Rev. B **23**, 3828 (1981).

[7]. T. Upton and W.A. Goddard, III, Phys. Rev. Lett. **46**, 1635 (1981); T.S. Rahman, J.E. Black and D.L. Mills, Phys. Rev. Lett. **46**, 1469 (1981).

[8]. S.Y. Tong and K.H. Lau, Phys. Rev. B **25**, 7382 (1982).

[9]. J. Stöhr, R. Jaeger and T. Kendelewicz, Phys. Rev. Lett. **49**, 142 (1982).

[10]. J.E. Demuth, N.J. DiNardo and G.S. Cargill, III, Phys. Rev. Lett. **50**, 1373 (1983).

[11]. J.W.M. Frenken, R.G. Smeenk, and J.F. Van Der Veen, Surf. Sci., **135,** 147 (1983).

[12]. L. Wenzel, D. Arvanitis, W. Daum, H.H. Rotermund, J. Stöhr, K. Baberschke, and H. Ibach, Phys. Rev. B **36**, 7689 (1987).

[13]. R.S. Saiki, A.P. Kaduwela, J. Osterwalder, C.S. Fadley, and C.R. Brundle, Phys. Rev. B **40**, 1586 (1989).

[14]. W.D. Wang, N.J. Wu, and P.A. Thiel, J. Chem. Phys. **92**, 2025 (1990).

[15]. S.R. Chubb, P.M. Marcus, K. Heinz and K. Muller, Phys. Rev. B **41**, 5417 (1990).

[16]. G. Wilhelmi, A. Brodde, D. Badt, H. Wengelnik, and H. Neddermeyer, Proceedings of the 1990 International Conf. on STM. (??Can Dick check exact reference?-not in JVST)

[17]. E. Kopatzki and R.J. Behm, Surf. Sci. **245**, 255 (1991).

[18]. T.D. Pope, S.J. Bushby, K. Griffiths, and P.R. Norton, Surf. Sci., in press.

[19]. (a) C.S. Fadley, Prog. Surf. Sci. **16**, 275 (1984); (b) Phys. Scr. **T17**, 39 (1987); (c) chapter in *Synchrotron Radiation Research: Advances in Surface Science*, edited by R.Z. Bachrach, (Plenum Press, New York, 1991), in press.

[20]. S.A. Chambers, I.M. Vitomirow, S.B. Anderson, H.W. Chen, T.J. Wagener, and J.H. Weaver, Superlatt. Microstruct. **3**, 563 (1987).

[21]. R.C. White, C.S. Fadley, and R. Trehan, J. Electron Spectrosc. Relat. Phenom. **41**, 95 (1986).

[22]. R.S. Saiki, A.P. Kaduwela, Y.J. Kim, D.J. Friedman, J. Osterwalder, S. Thevuthasan and C.S. Fadley, to be published.

[23]. J. Osterwalder, M. Sagurton, P.J. Orders, C.S. Fadley, B.D. Hermsmeier and D.J. Friedman, J. Electron Spectrosc. Relat. Phenom. **48**, 55 (1989).

[24]. R.J. Baird and C.S. Fadley, J. Electron Spectrosc. Relat. Phenom., **11**, 39 (1977); R.J. Baird, Ph.D. Thesis (University of Hawaii, 1977).

[25]. S.M. Goldberg, C.S. Fadley and S. Kono, J. Electron Spectrosc. Relat. Phenom. **21**, 285 (1981); J.J. Yeh and I. Lindau, Atomic Data and Nuclear Data Tables, **32**, 1 (1985).

[26]. (a) C.J. Powell, Surf Sci. **44**, 29 (1974); (b) M.P. Seah and W.A. Dench, Surf. Interface Anal. **1**, 2 (1979); (c) R.E. Connelly, C.S. Fadley, and P.J. Orders, J. Vac. Sci. Technol. **A2**, 1333 (1984). The mean free path Λ_e^m(629 eV) for Ni $2p_{3/2}$ was taken to be 10.0 Å for the clean metal and assumed to scale as $E_{kin}^{0.52}$ in the oxide, leading to a value of Λ_e^{ox}(954 eV) = 12.3 Å.

[27]. D.R. Penn, J. Electron Spectrosc. Relat. Phenom. **9**, 29 (1976).

[28]. H. Hopster and C.R. Brundle, unpublished results.

[29]. R.S. Saiki, Ph.D. Thesis (University of Hawaii, 1991). Typical XPS spectra from the clean and oxidized surface are presented here.

[30]. R.B. Hall, C.A. Mims, J.H. Hardenbergh, and J.G Chen, to be published.

[31]. (a) J.J. Rehr and R.C. Albers, Phys. Rev. B **41**, 8139 (1990); (b) D.J. Friedman and C.S. Fadley, J. Electron Spectrosc. Relat. Phenom. **51**, 689 (1990).

[32]. A.P. Kaduwela, G.S. Herman, D.J. Friedman, C.S. Fadley, and J.J. Rehr, Phys. Scri. **41**, 948 (1990).

[33]. A.P. Kaduwela, D.J. Friedman and C.S. Fadley, J. Electron Spectrosc. Relat. Phenom., in press.

[34]. L.F. Mattheiss, Phys. Rev. B **5**, 290 (1972).

[35]. M.A. Van Hove, S.Y. Tong and M.H. Elconin, Surf. Sci. **64**, 85 (1977). In the present work, a new type of normalization of theory and experiment more appropriate to XPD is used, but the definitions of R_1, R_2, R_3, R_4, and R_5 are the same as in this paper.

[36]. E. Zanazzi and F. Jona, Surf. Sci., **62**, 61 (1977).

[37]. E.L. Bullock and C.S. Fadley, Phys. Rev. B **31**, 1212 (1985).

[38]. J. Osterwalder, E.A. Stewart, D. Cry, C.S. Fadley, J. Mustre de Leon, and J.J. Rehr, Phys. Rev. B **35**, 9859 (1987); J. Osterwalder, A. Stuck, D.J. Friedman, A. Kaduwela, C.S. Fadley, J. Mustre de Leon, and J.J. Rehr, Phys. Scr. **41**, 990 (1990).

[39]. (a) S. Andersson and J.B. Pendry, Sol. St. Commun. **16**, 563 (1975); (b) M.A. Van Hove, W.H. Weinberg, and C.-M. Chan in *Low Energy Electron Diffraction, Experiment, Theory and Surface Structure Determination*, edited by G. Ertl, (Springer-Verlag, Berlin 1986), Vol 6, pp. 246-248.

Table 1

Values of z and d_{12} from selected techniques. The multilayer LEED result changes to z = 0.85 Å if the d_{12} spacing is fixed at the bulk value of 1.76 Å.

Parameter	XPD	Multilayer LEED	Total Energy	ARPEFS	SEXAFS	ISS
z	0.75±0.05 Å	0.75±0.04 Å	0.84±0.01 Å	0.90±0.04 Å	0.88±0.04 Å	0.86±0.1 Å
d_{12}	——	1.86±0.02 Å	1.76 Å(fixed)	——	——	1.85±0.03 Å
Reference	[a]	[b]	[b]	[c]	[d]	[e]

[a] This work

[b] Reference 15

[c] Reference 6

[d] Reference 12

[e] Reference 11

FIGURE CAPTIONS:

Figure 1. A schematic of the principle surface structures that appear on Ni(001) under ambient-temperature oxygen exposures from approximately 30 L up the 1200 L. (a) Very rapid atomic O adsorption leading to a c(2×2) overlayer. The c(2×2) structure results in a temporary reduction of the oxygen uptake as all available dissociation/chemisorption sites are filled. (b) Formation of small oxide nuclei well before the ideal c(2×2) coverage of 0.50 ML is reached. At ambient temperature, these islands are thought to be predominantly NiO in the [001] orientation and they have been estimated to be between 2- and 3-ML thick. (c) Continued lateral growth at the oxide perimeters on additional oxygen exposure in the range of 70 to 600 L and a corresponding reduction in the c(2×2) structure. (d) Saturation of the oxide overlayer is reached at ~1200 L and two, very distinct epitaxial orientations have been detected. The majority oxide is in the (001)-orientation, while a minority (111) species has also been observed. (e) Annealing briefly to 523 K for about five minutes results in a vertical thickening of the oxide islands and the appearance of oxygen-depleted regions indicated by the reappearance of the c(2×2) structure.

Figure 2. General geometry of our experiment, showing the directions of the polar (θ) and azimuthal (ϕ) specimen rotations. The angle α was fixed at 72° for the HP spectrometer and at 48° for the VG spectrometer. Al Kα radiation ($h\nu$ =1486.6 eV) was used in either case. The surface normal of the specimen is the [001] direction of nickel, and ϕ is measured with respect to [100].

Figure 3. (a) XPS oxygen coverage data (solid curve) as a function of oxygen exposure and associated LEED observations from the clean surface up to 1200 L. Also shown are the O/Ni Auger ratio data of Wang *et al.* (dashed curves) at substrate temperatures between

300 K and 400 K. The Auger curves have been normalized so that the result at 400 K crosses the XPS curve at 30 L. The XPS observation direction was chosen to represent an average Ni $2p_{3/2}$ intensity from the surface and thus to avoid the enhancement of photoemission intensity commonly found along low-index rows of atoms. The XPS coverages here do not allow for attenuation in the oxide overlayer, and thus represents lower bounds. (b) As in (a), but a close-up of the critical 0 L to 120 L region that spans the c(2×2) overlayer regime.

Figure 4. Two of the primary surface structures of interest here are: (a) the fourfold-hollow c(2×2) structure occurring at submonolayer coverages of less than ~0.5 ML and (b) the saturated oxide in (001) orientation, which forms at coverages of 2-ML or more. Grazing electron emission angles were used to obtain surface-sensitive diffraction information, while larger takeoff angles were used to probe the deeper subsurface structures, especially of the second and deeper lying oxygen emitters of the oxide.

Figure 5. (a) A schematic drawing of an ideal 2-ML of NiO(001) grown on Ni(001), with the oxide overlayer having a lattice constant parallel to the surface that is expanded by $^1/_6$ relative to the underlying Ni(001) substrate. The two bold arrows correspond to oxygen forward scattering along the [101] emission directions at a polar angle $\theta = 45°$, and to nickel forward scattering along the $[1\bar{1}1]$ directions at $\theta = 35.3°$. (b) Two types of clusters used in our theoretical analysis: an intermediate-sized 35-atom cluster, 2-ML thick, that spans approximately two unit cells, and a minimal five-atom cluster (one emitter plus four scatterers) shown here as those atoms with the heavier outline.

Figure 6. Experimental O 1s azimuthal scans taken along $\theta = 36.3°$ (very close to the $<1\bar{1}1>$ direction at 35.3°), with a standard angular resolution of ±3.0° and for a series of

oxygen exposures from c(2×2) at 30 L up to the saturated oxide at 1200 L. These curves are compared to SSC calculations for fourfold hollow c(2×2) oxygen at $z = 0.75$ Å and for saturated oxide made up of 2-ML of NiO(001) having various cluster sizes to explore the effect of domain size and strain on the diffraction patterns. Also shown is the calculated diffraction pattern for 2-ML of NiO(111) having long range order.

Figure 7. Same as Figure 6, but for $\theta = 46°$, which is close to the <101> direction at $\theta = 45°$.

Figure 8. (a) Experimental polar scans of the O 1s intensity along the <101> azimuth, obtained under high angular resolution of ±1.5° before and after a quick anneal of the saturated oxide to 523 K, are compared to theoretical diffraction calculations for a variety of clusters. The position of the forward scattering peak along the <101> direction is used to determine the interplanar separation of the oxide in the NiO(001) overlayer. (b) As (a) but along the $<1\bar{1}1>$ azimuth.

Figure 9. Experimental fourfold-averaged O 1s azimuthal scans of the unannealed saturated oxide at $\theta = 43°$, 45°, and 47° are compared to theoretical calculations for intermediate-size 35-atom clusters incorporating various structural distortions as described in the text, as well as for a minimal five-atom cluster.

Figure 10. Sums of R_1 R-factors comparing different theoretical calculations to the five azimuthal scans at $\theta = 43°$, 44°, 45°, 46°, and 47° for the unannealed oxide data summarized in Figure 9.

Figure 11. High angular resolution O 1s azimuthal experimental data from an annealed oxide overlayer for five closely spaced polar angles near [101].

Figure 12. Similar to Figure 9, but after a quick anneal to 523 K and obtained with a high angular resolution of ±1.5°. Theoretical calculations are for fully converged clusters of 20 Å in radius that were found to be necessary in order to predict all of the diffraction features present.

Figure 13. Summed R_1 results similar to Figure 10, but this time for the high angular resolution annealed oxide azimuthal data of Figures 11 and 12.

Figure 14. Experimental azimuthal scans of the O 1s intensity for c(2×2) oxygen (30 L) and the unannealed saturated oxide (1200 L) at (a) $\theta = 8°$ and (b) $\theta = 11°$. These curves are compared to SSC calculations for the c(2×2) overlayer residing in the fourfold hollow at z = 0.75 Å and for the oxide to calculations for a 35-atom cluster having an a_{12} expansion of +0.2 Å, as well as for a 2-ML NiO(001) cluster of 10 Å in radius.

Figure 15. As Figure 14, but for (a) $\theta = 14°$ and (b) $\theta = 17°$.

Figure 16. Summed R_1 results for the unannealed oxide azimuthal data shown in Figures 14 and 15.

Figure 17. (a) Summed R_1 results comparing the c(2×2) azimuthal data taken at the grazing emission angles of $\theta = 8°$ and 11° to theoretical calculations comparing the fourfold hollow and the pseudobridge bonding site. (b) Comparison of all five summed R-factors for the fourfold hollow site. (See definitions of R_1, R_2, R_3, R_4, and R_5 in the text.)

Figure 18. Comparison of experimental and theoretical azimuthal curves for the c(2×2)O structure at $\theta = 8°$ and 11°. Theoretical curves are for the optimal geometry based on the R_1 analysis of the fourfold hollow ($z = 0.75$ Å) and for the pseudobridge site proposed by Demuth *et al.*.

Figure 19. (a) and (c) Height-dependent R-factor analysis comparing experiment to the fully converged fourfold hollow theory at $\theta = 8°$ and 11°, respectively. The downward pointing arrows indicate the expected positions of the different orders of constructive interference between the direct wave and a wave singly scattered from the nearest-neighbor Ni atom, as calculated from Equation (6). (b) and (d) Analogous R-factor comparisons of theory to theory in which only the nearest-neighbor Ni scatterer is present in a two-atom cluster. In (b), the two-atom curve at $z = 0.8$ Å is used as the reference, and in (d) the curve at $z = 0.7$ Å is used.

Figure 20. Geometry of the nearest-neighbor scattering interaction, illustrating the pathlength difference involved in producing the oscillations in Figure 19.

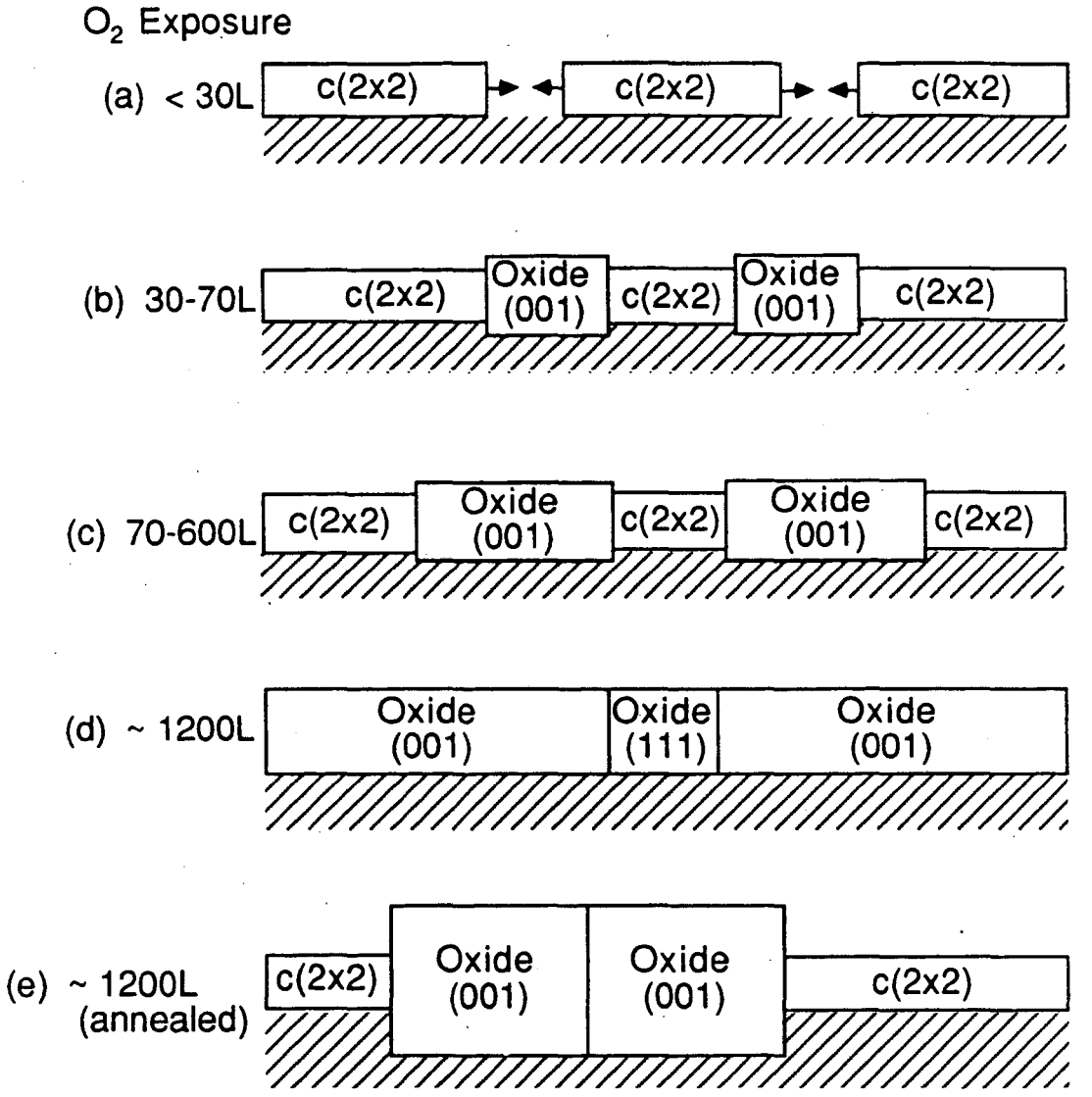

XBL 927-1652

Figure 1

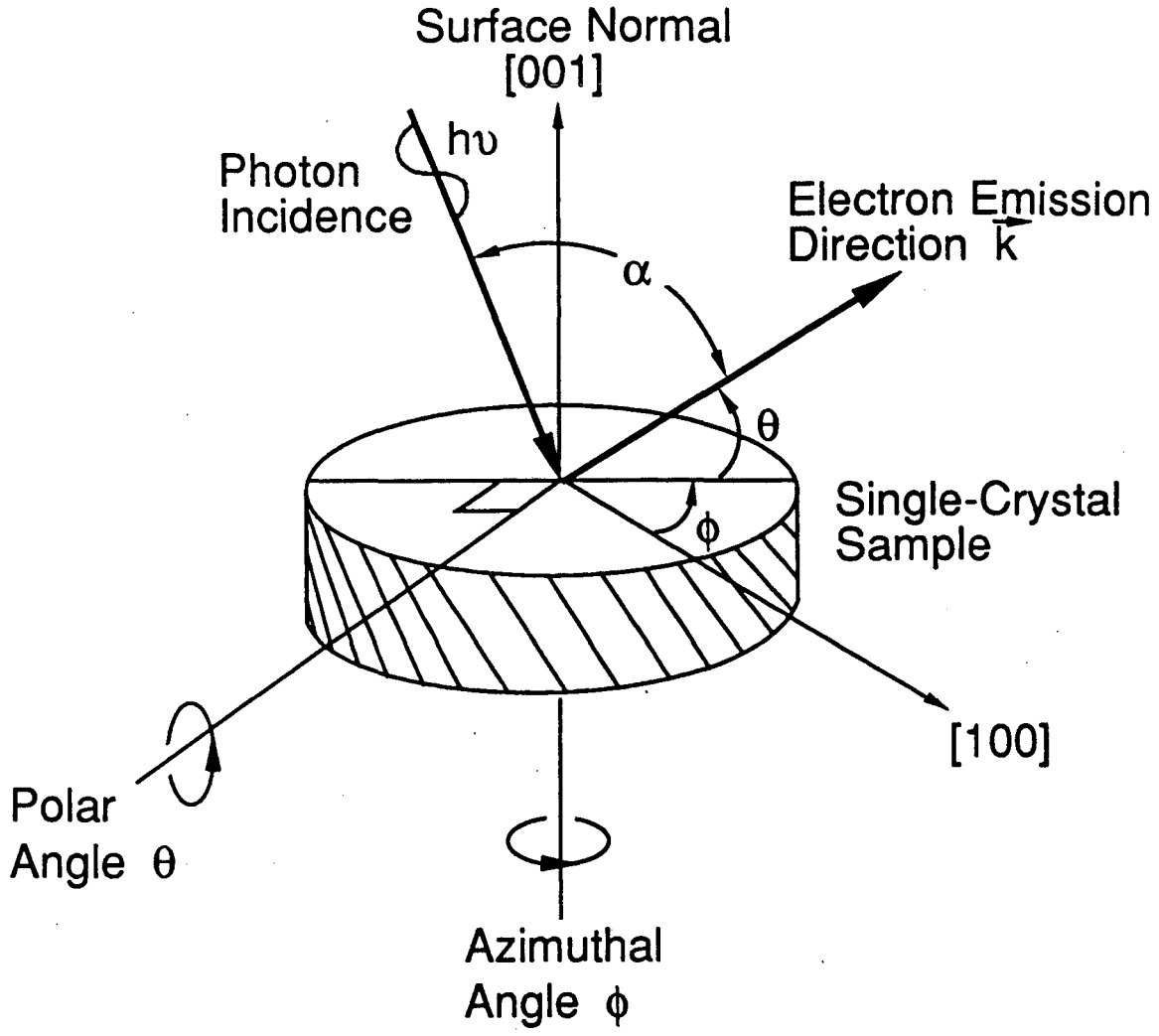

XBL 927-1653

Figure 2

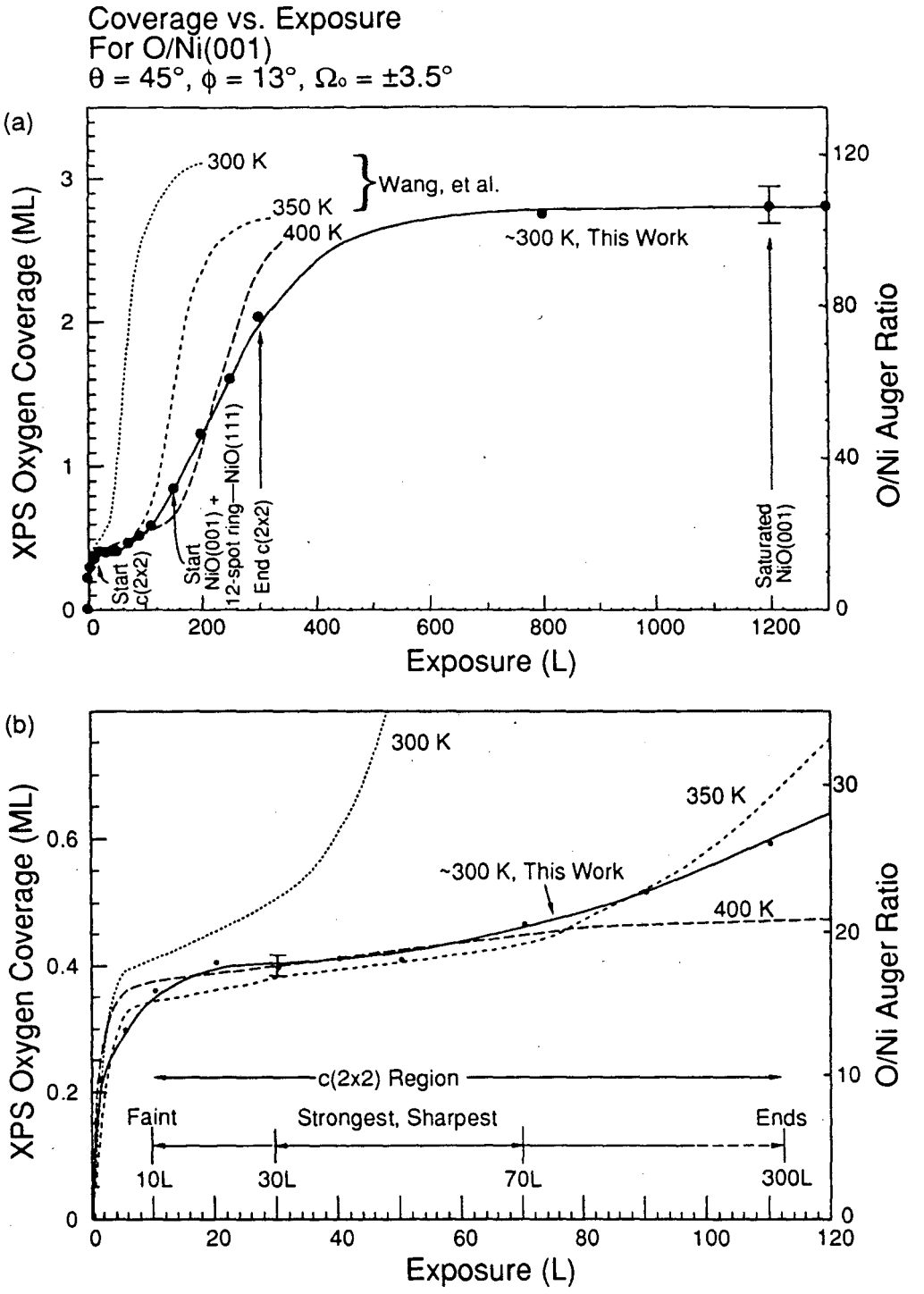

Figure 3

XBL 927-1654

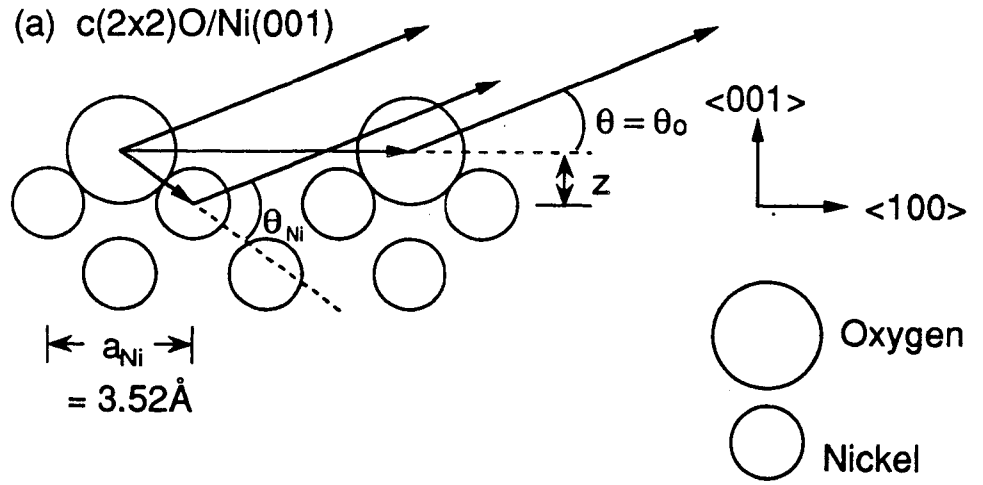

(b) 3 ML of NiO(001)

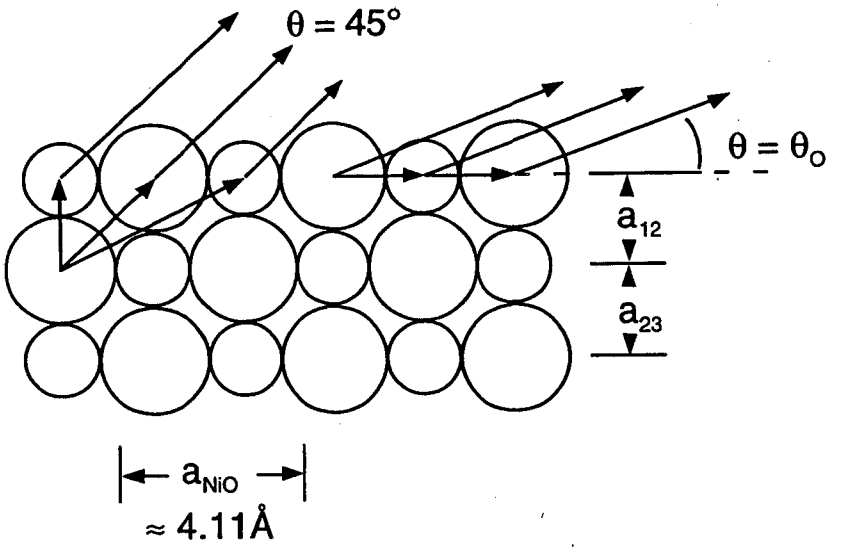

XBL 927-1655

Figure 4

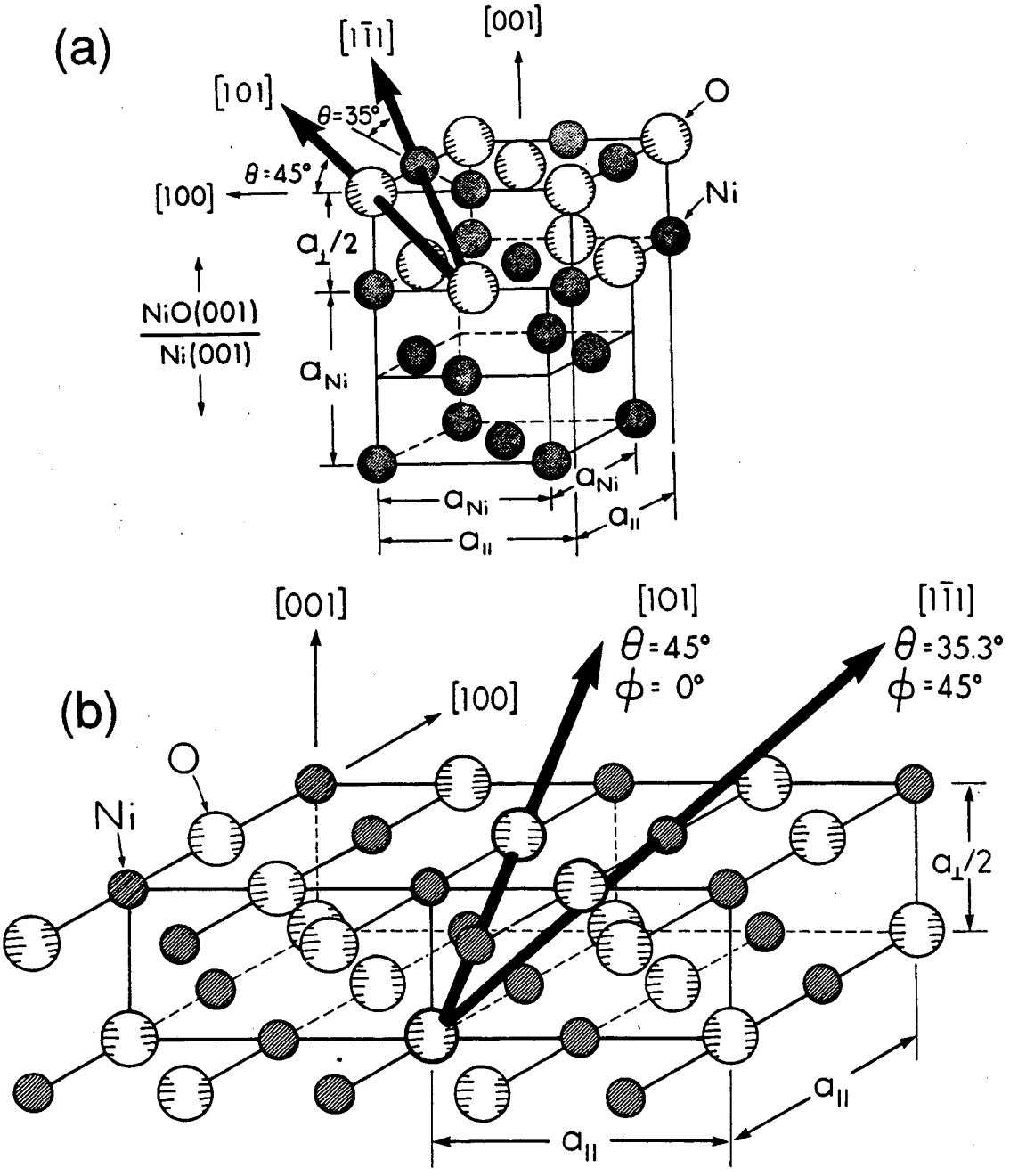

XBL 927-1656

Figure 5

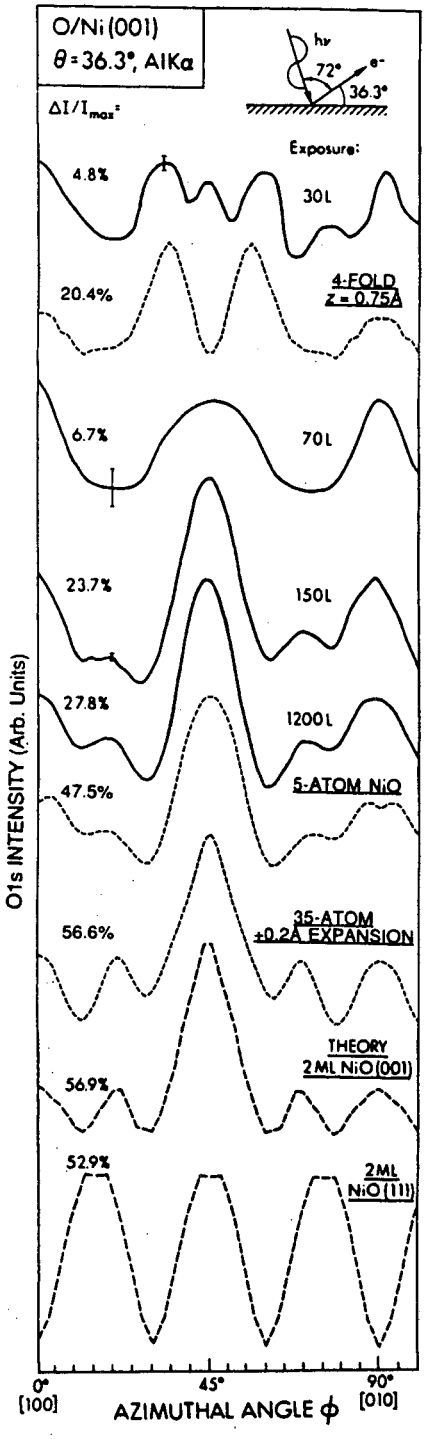

XBL 927-1657

Figure 6

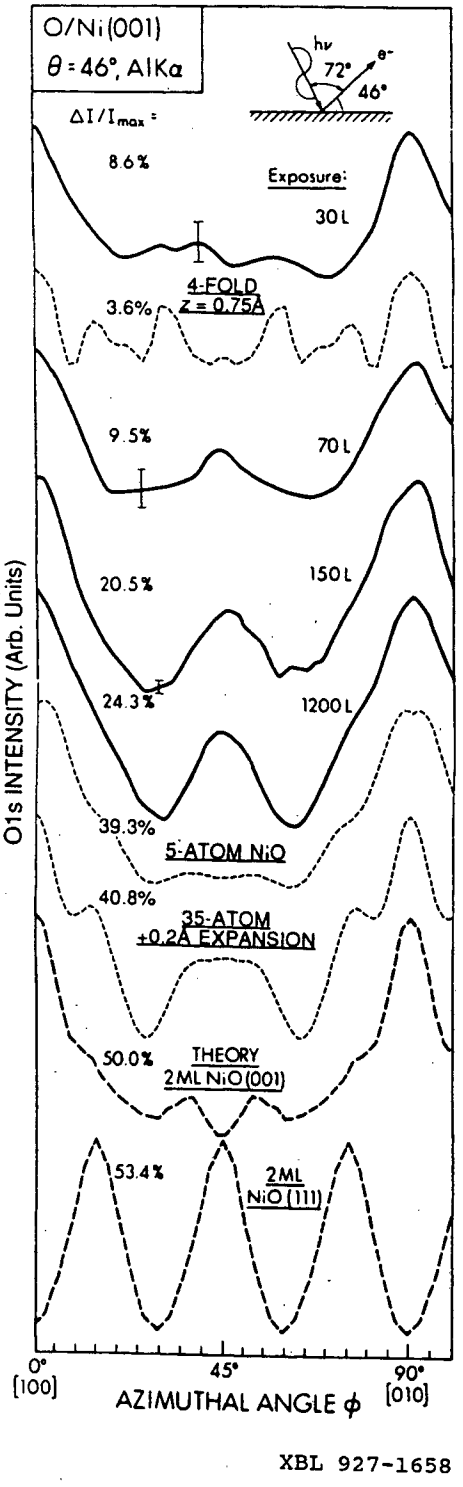
O/Ni(001)
θ = 46°, AlKα
hν
72°
e⁻
46°
ΔI/I_max =
8.6%
Exposure:
30 L
4-FOLD
z = 0.75Å
3.6%
9.5%
70 L
20.5%
150 L
24.3%
1200 L
39.3%
5-ATOM NiO
40.8%
35-ATOM
+0.2Å EXPANSION
50.0%
THEORY
2ML NiO(001)
53.4%
2ML
NiO(111)
O1s INTENSITY (Arb. Units)
0°
[100]
45°
90°
[010]
AZIMUTHAL ANGLE φ
XBL 927-1658

Figure 7

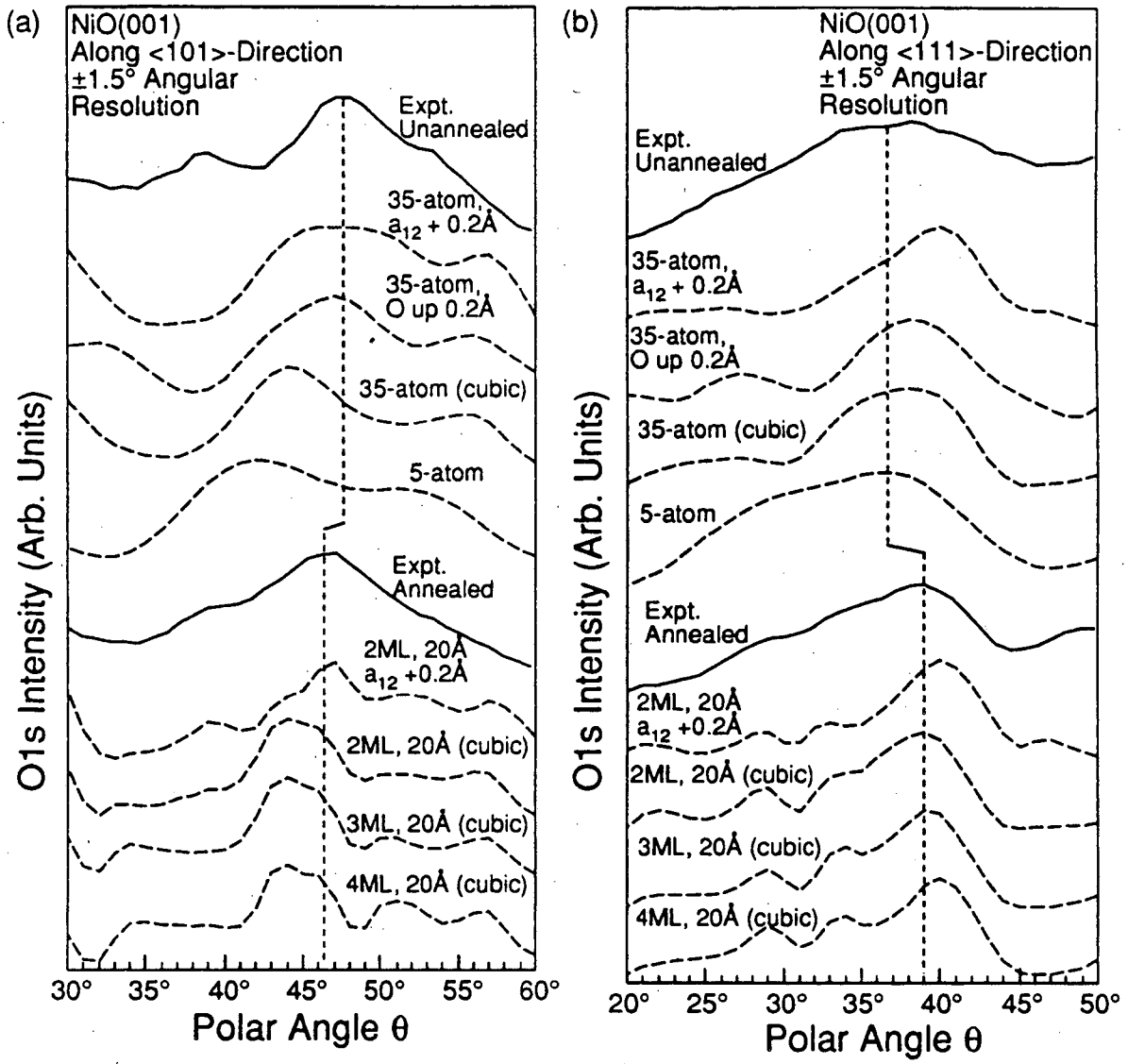
(a)
NiO(001)
Along <101>-Direction
±1.5° Angular
Resolution
Expt.
Unannealed
35-atom,
a_{12} + 0.2Å
35-atom,
O up 0.2Å
35-atom (cubic)
5-atom
Expt.
Annealed
2ML, 20Å
a_{12} +0.2Å
2ML, 20Å (cubic)
3ML, 20Å (cubic)
4ML, 20Å (cubic)
O1s Intensity (Arb. Units)
30° 35° 40° 45° 50° 55° 60°
Polar Angle θ
(b)
NiO(001)
Along <111>-Direction
±1.5° Angular
Resolution
Expt.
Unannealed
35-atom,
a_{12} + 0.2Å
35-atom,
O up 0.2Å
35-atom (cubic)
5-atom
Expt.
Annealed
2ML, 20Å
a_{12} +0.2Å
2ML, 20Å (cubic)
3ML, 20Å (cubic)
4ML, 20Å (cubic)
O1s Intensity (Arb. Units)
20° 25° 30° 35° 40° 45° 50°
Polar Angle θ
XBL 927-1659

Figure 8

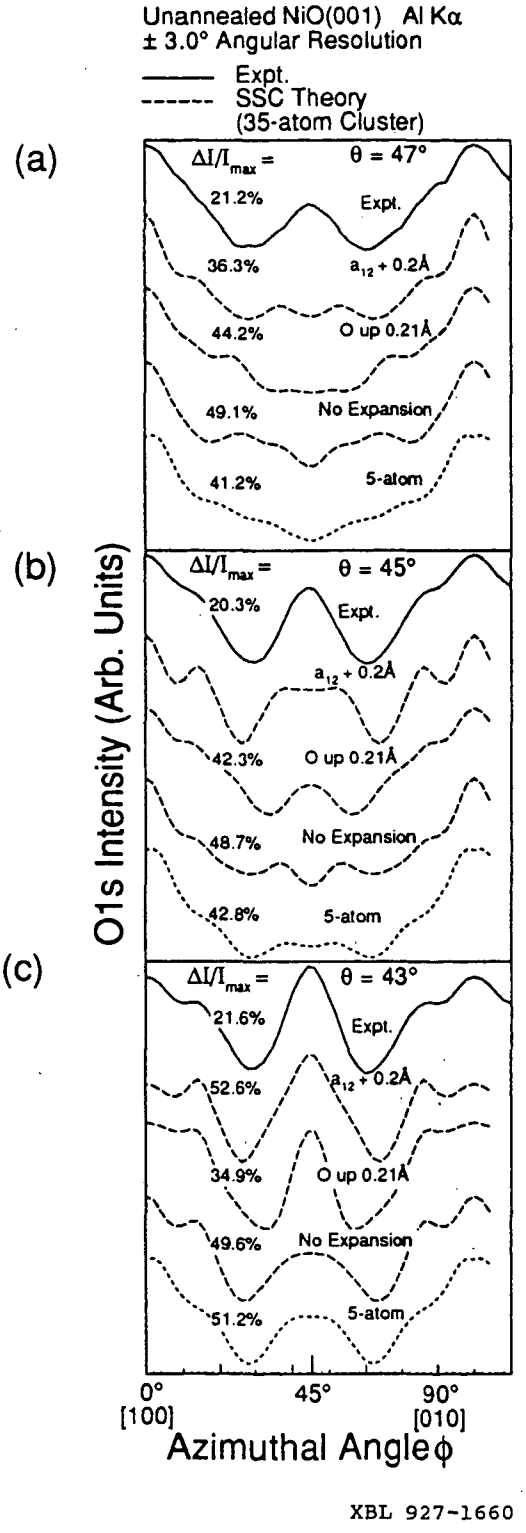
Unannealed NiO(001) Al Kα
± 3.0° Angular Resolution
Expt.
SSC Theory
(35-atom Cluster)
(a)
ΔI/I_max =
θ = 47°
21.2%
Expt.
36.3%
a12 + 0.2Å
44.2%
O up 0.21Å
49.1%
No Expansion
41.2%
5-atom
(b)
ΔI/I_max =
θ = 45°
20.3%
Expt.
a12 + 0.2Å
42.3%
O up 0.21Å
48.7%
No Expansion
42.8%
5-atom
(c)
ΔI/I_max =
θ = 43°
21.6%
Expt.
52.6%
a12 + 0.2Å
34.9%
O up 0.21Å
49.6%
No Expansion
51.2%
5-atom
O1s Intensity (Arb. Units)
0°
[100]
45°
90°
[010]
Azimuthal Angle ϕ
XBL 927-1660

Figure 9

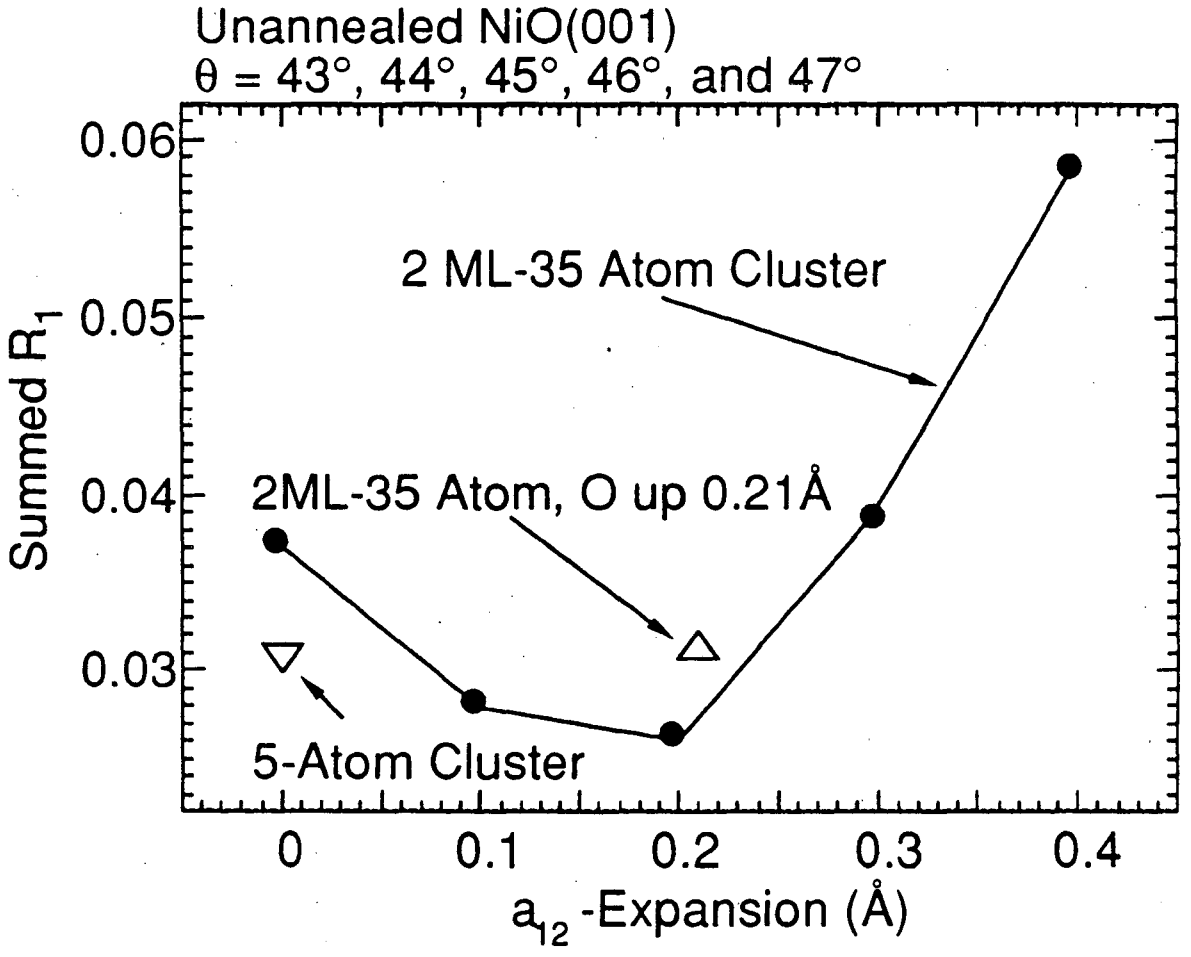
Unannealed NiO(001)
θ = 43°, 44°, 45°, 46°, and 47°
Summed R_1
0.06
0.05
0.04
0.03
2 ML-35 Atom Cluster
2ML-35 Atom, O up 0.21Å
5-Atom Cluster
0
0.1
0.2
0.3
0.4
a_{12} -Expansion (Å)
XBL 927-1661

Figure 10

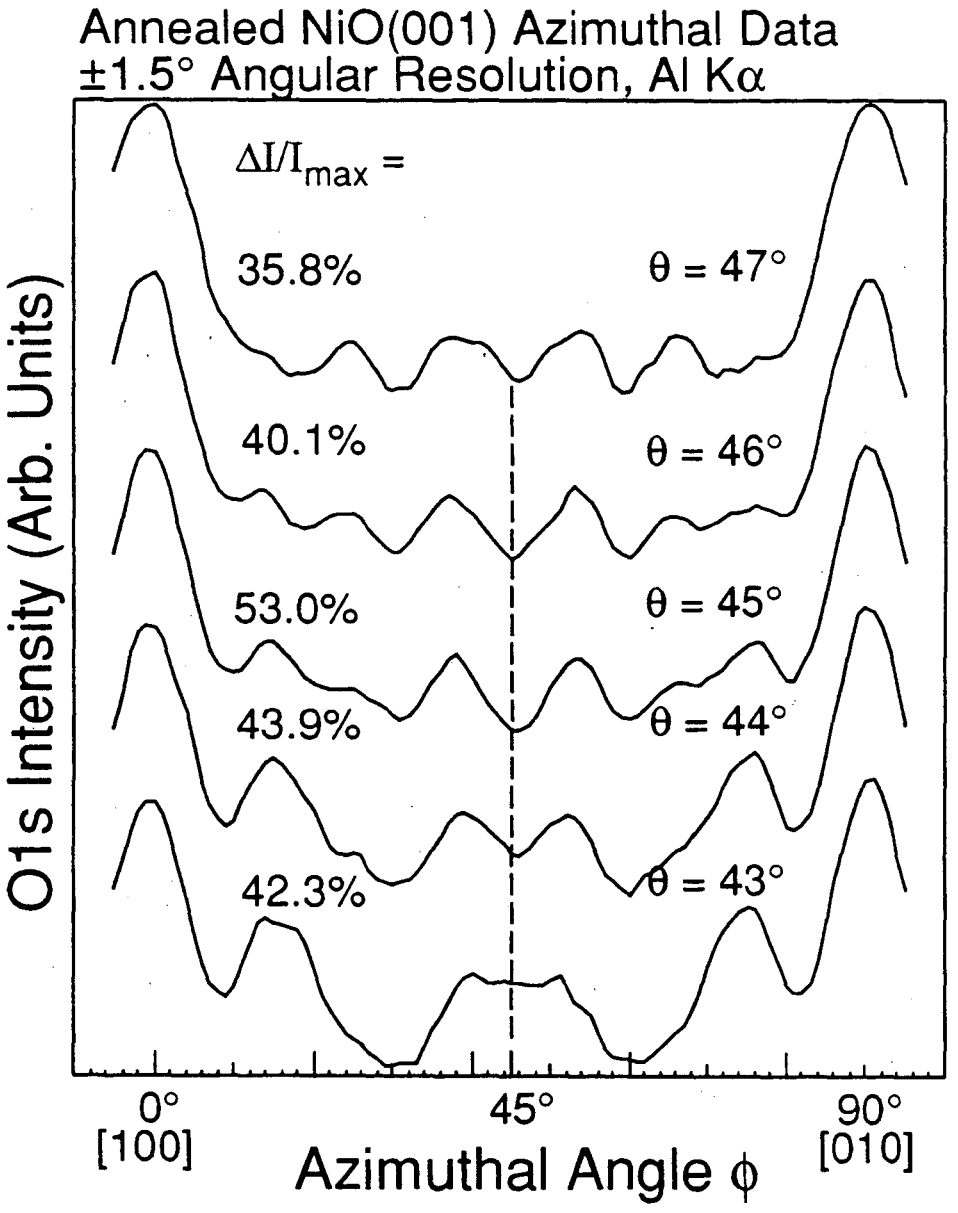
Annealed NiO(001) Azimuthal Data
±1.5° Angular Resolution, Al Kα
ΔI/I_max =
35.8%
θ = 47°
40.1%
θ = 46°
53.0%
θ = 45°
43.9%
θ = 44°
42.3%
θ = 43°
O1s Intensity (Arb. Units)
0°
[100]
45°
90°
[010]
Azimuthal Angle ϕ
XBL 927-1662

Figure 11

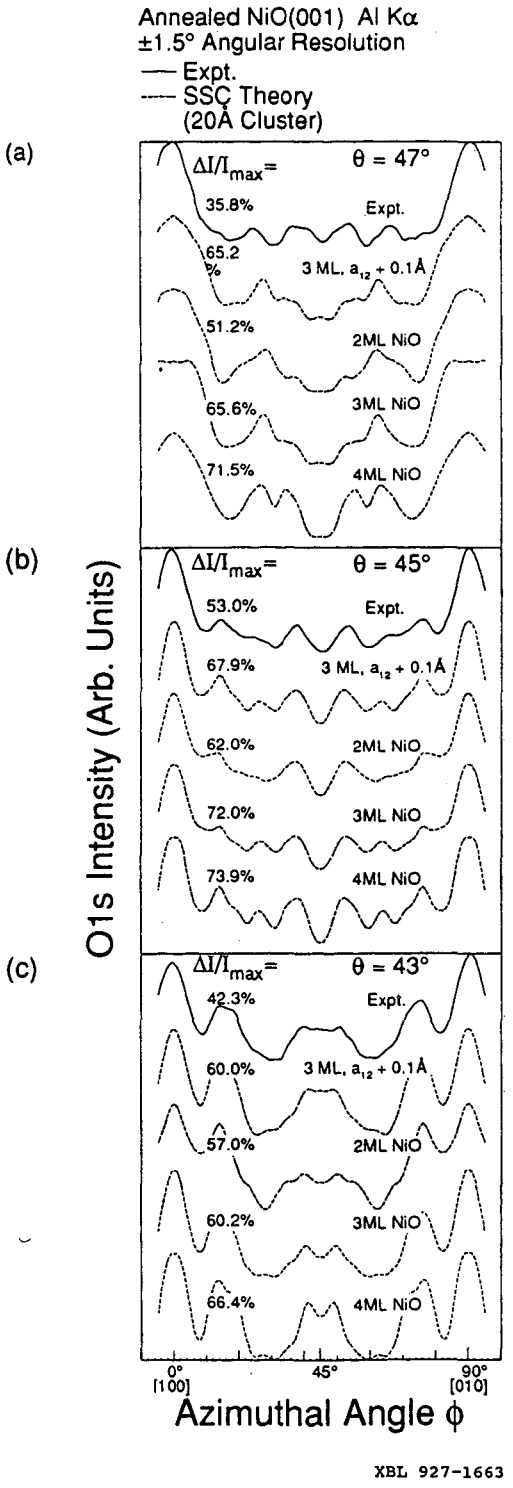
Annealed NiO(001) Al Kα
±1.5° Angular Resolution
— Expt.
---- SSC Theory
(20Å Cluster)
(a)
ΔI/I_max=
θ = 47°
35.8%
Expt.
65.2 %
3 ML, a_12 + 0.1Å
51.2%
2ML NiO
65.6%
3ML NiO
71.5%
4ML NiO
(b)
ΔI/I_max=
θ = 45°
53.0%
Expt.
67.9%
3 ML, a_12 + 0.1Å
62.0%
2ML NiO
72.0%
3ML NiO
73.9%
4ML NiO
(c)
ΔI/I_max=
θ = 43°
42.3%
Expt.
60.0%
3 ML, a_12 + 0.1Å
57.0%
2ML NiO
60.2%
3ML NiO
66.4%
4ML NiO
O1s Intensity (Arb. Units)
0°
[100]
45°
90°
[010]
Azimuthal Angle ϕ
XBL 927-1663

Figure 12

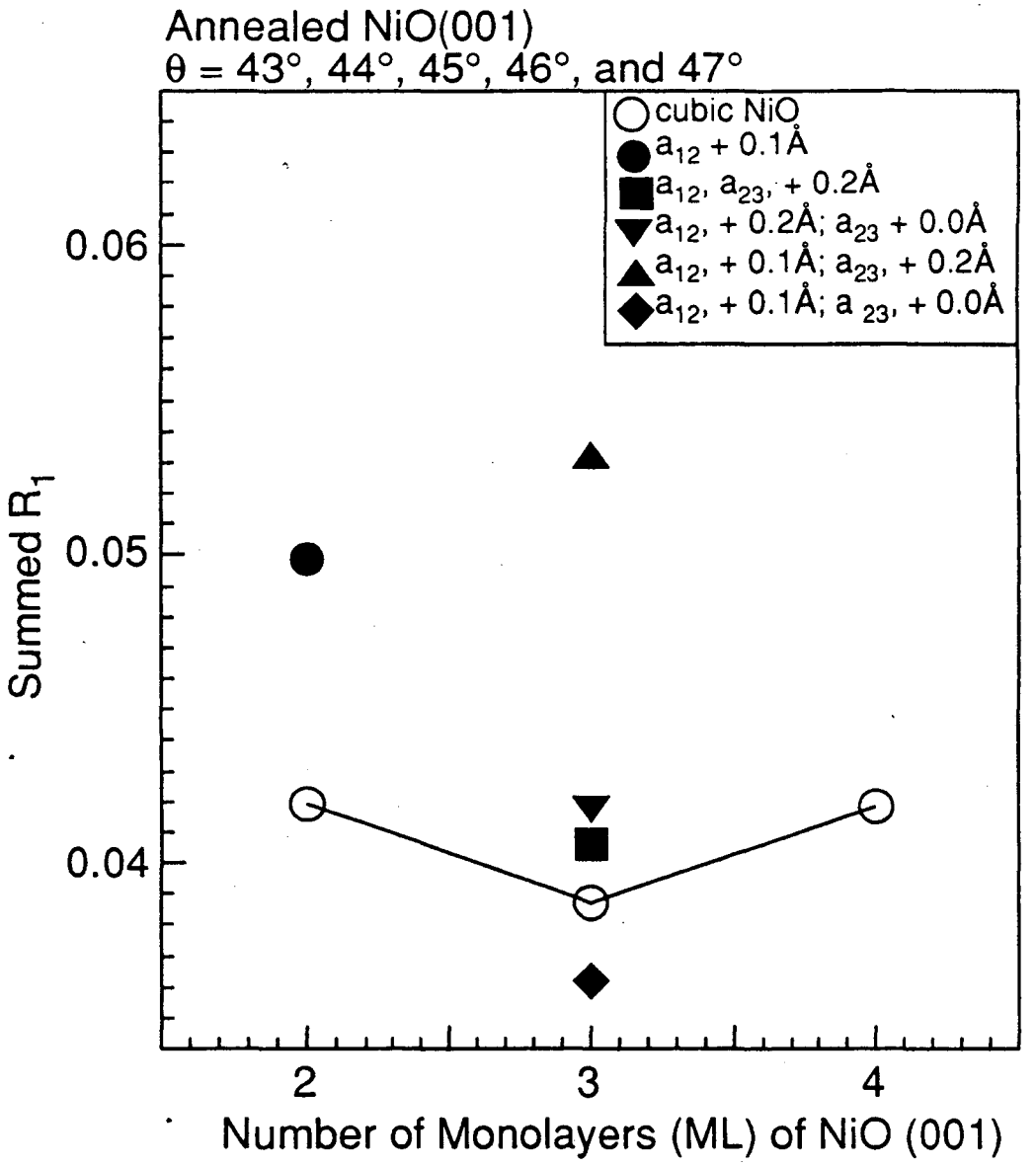

XBL 927-1664

Figure 13

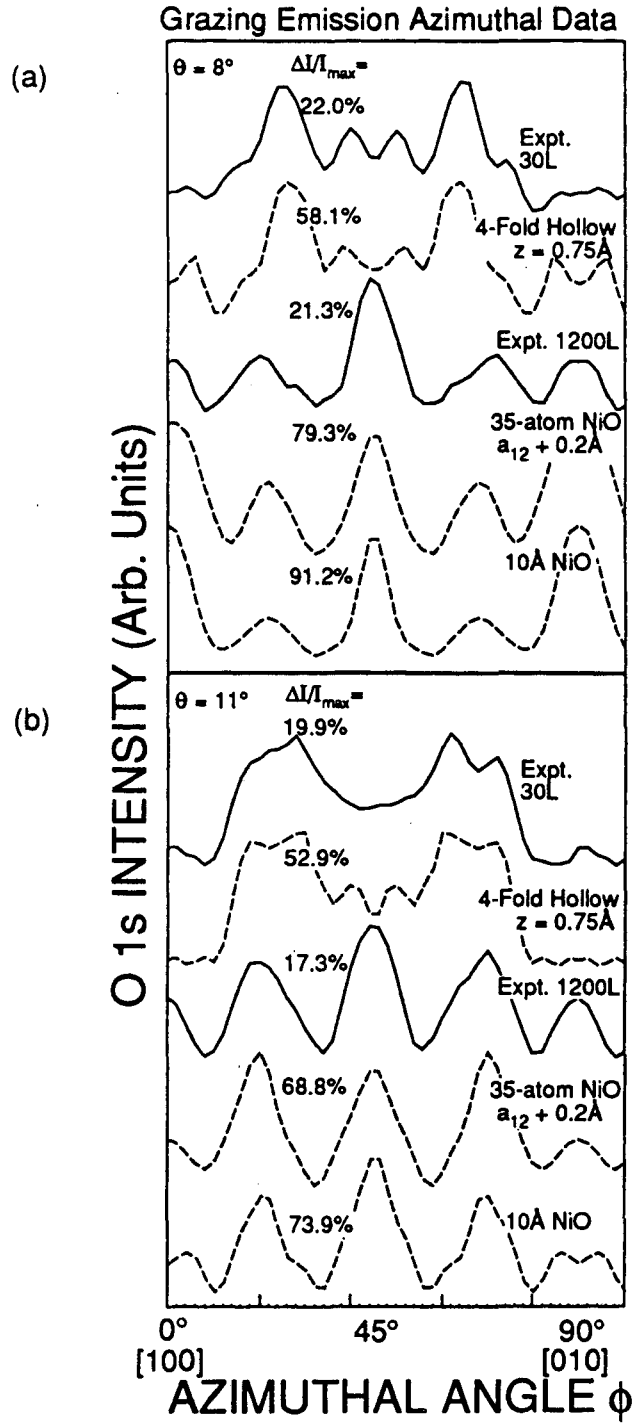

XBL 927-1665

Figure 14

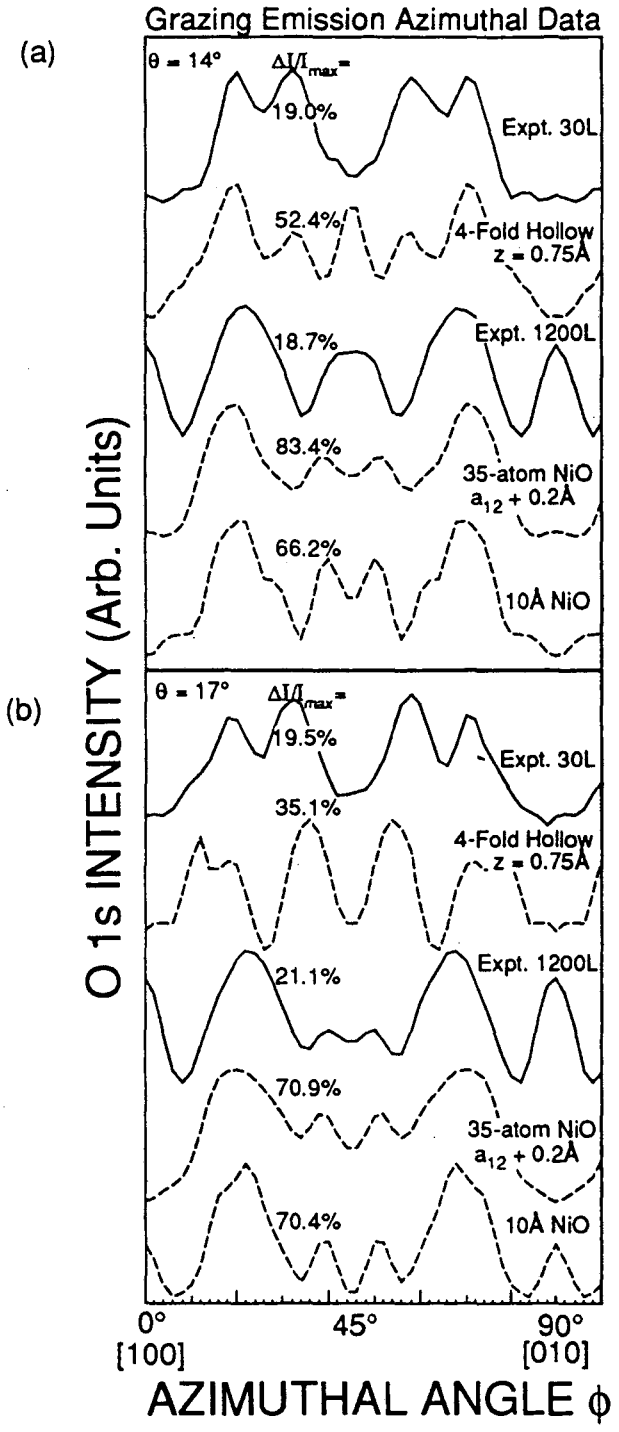
Grazing Emission Azimuthal Data
(a)
θ = 14°
ΔI/I max =
19.0%
Expt. 30L
52.4%
4-Fold Hollow
z = 0.75Å
18.7%
Expt. 1200L
83.4%
35-atom NiO
a12 + 0.2Å
66.2%
10Å NiO
(b)
θ = 17°
ΔI/I max =
19.5%
Expt. 30L
35.1%
4-Fold Hollow
z = 0.75Å
21.1%
Expt. 1200L
70.9%
35-atom NiO
a12 + 0.2Å
70.4%
10Å NiO
O 1s INTENSITY (Arb. Units)
0°
[100]
45°
90°
[010]
AZIMUTHAL ANGLE ϕ
XBL 927-1666

Figure 15

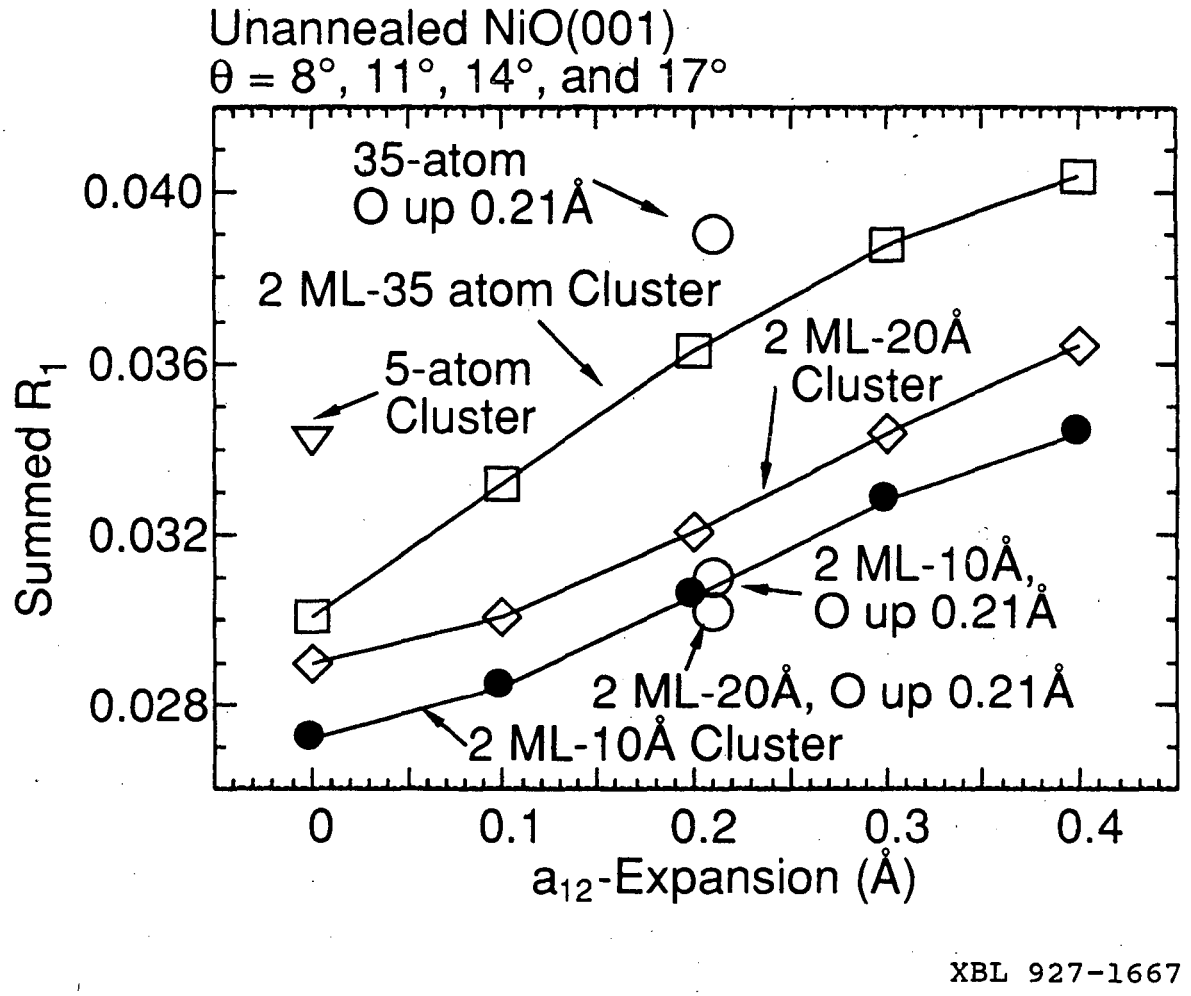
Unannealed NiO(001)
θ = 8°, 11°, 14°, and 17°
35-atom
O up 0.21Å
2 ML-35 atom Cluster
5-atom
Cluster
2 ML-20Å
Cluster
2 ML-10Å,
O up 0.21Å
2 ML-20Å, O up 0.21Å
2 ML-10Å Cluster
Summed R_1
0.040
0.036
0.032
0.028
0
0.1
0.2
0.3
0.4
a_{12}-Expansion (Å)
XBL 927-1667

Figure 16

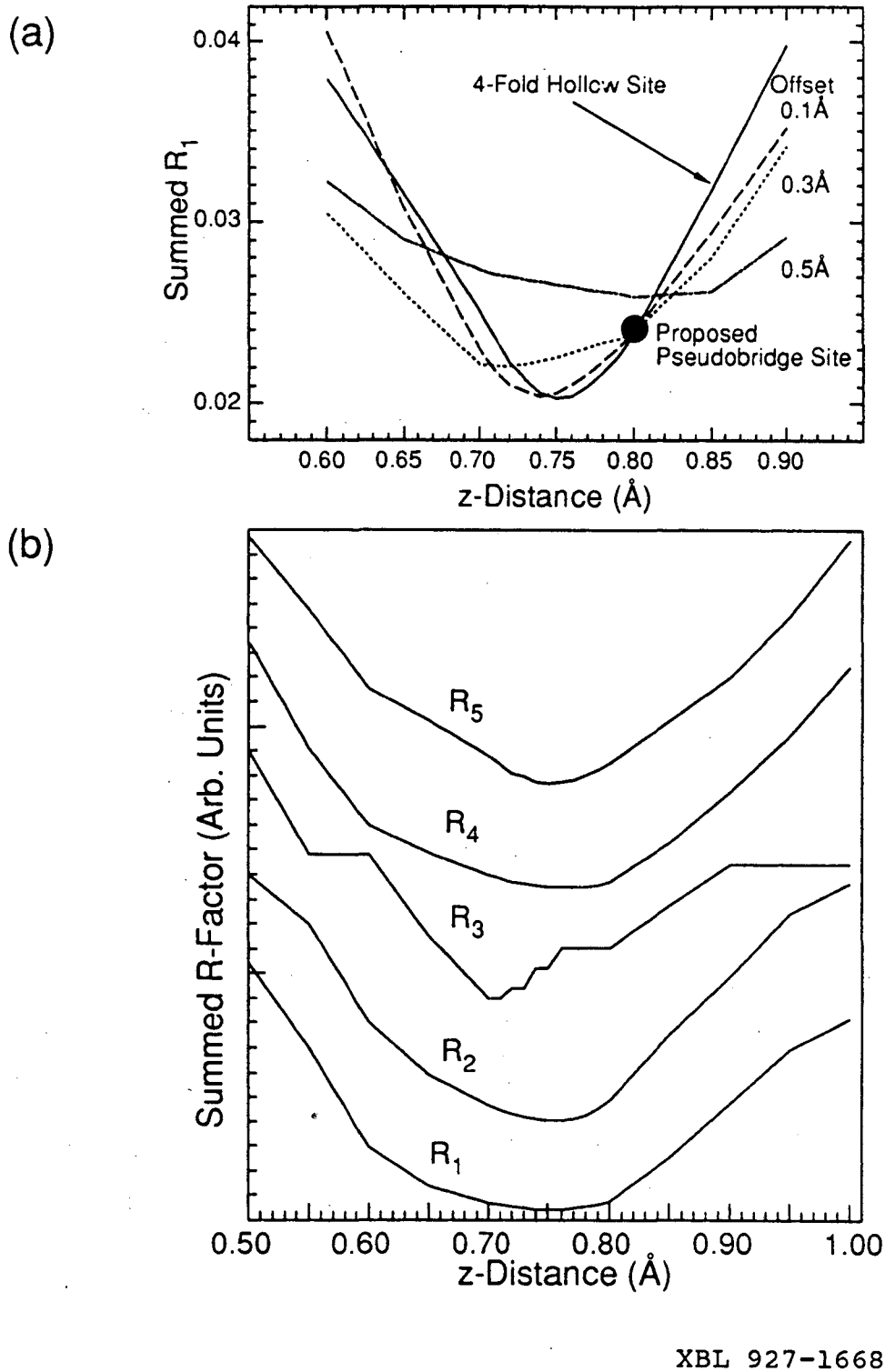

XBL 927-1668

Figure 17

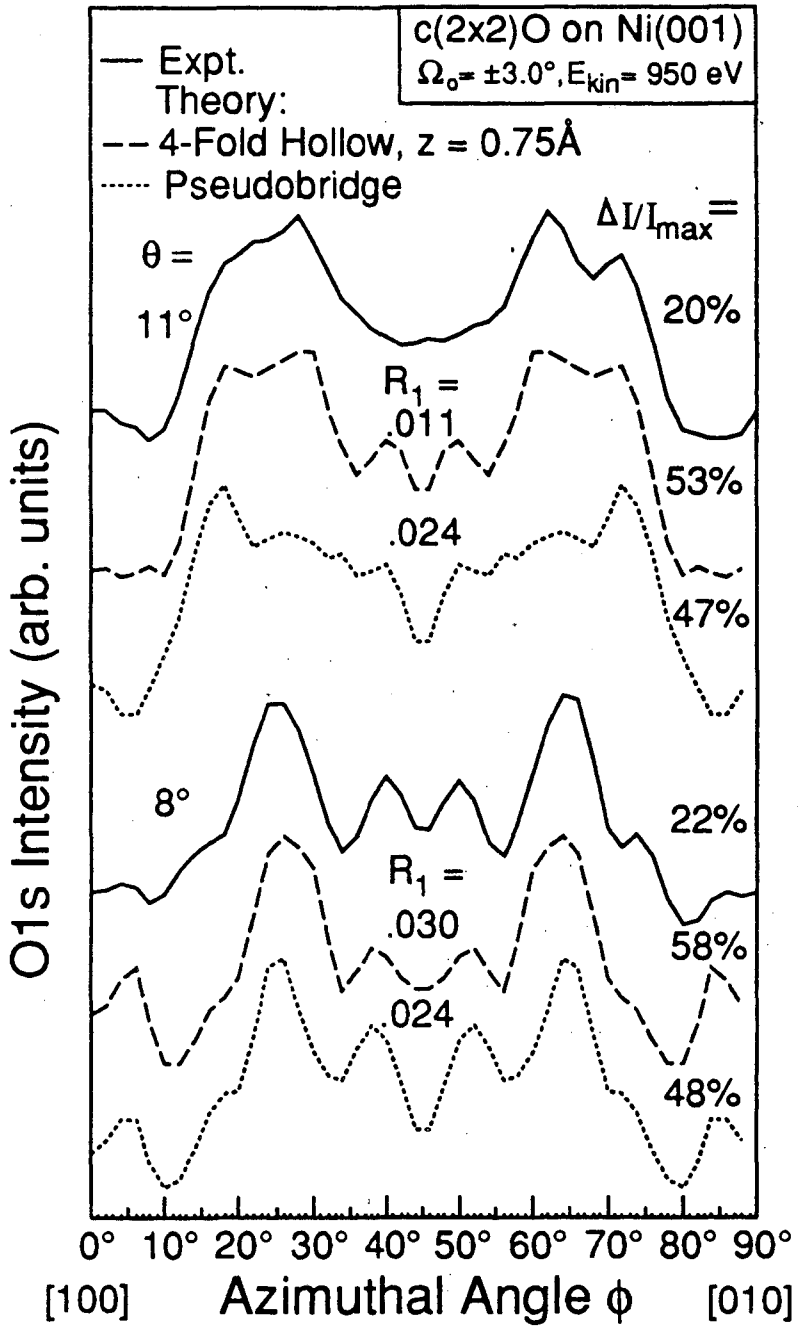

XBL 927-1669

Figure 18

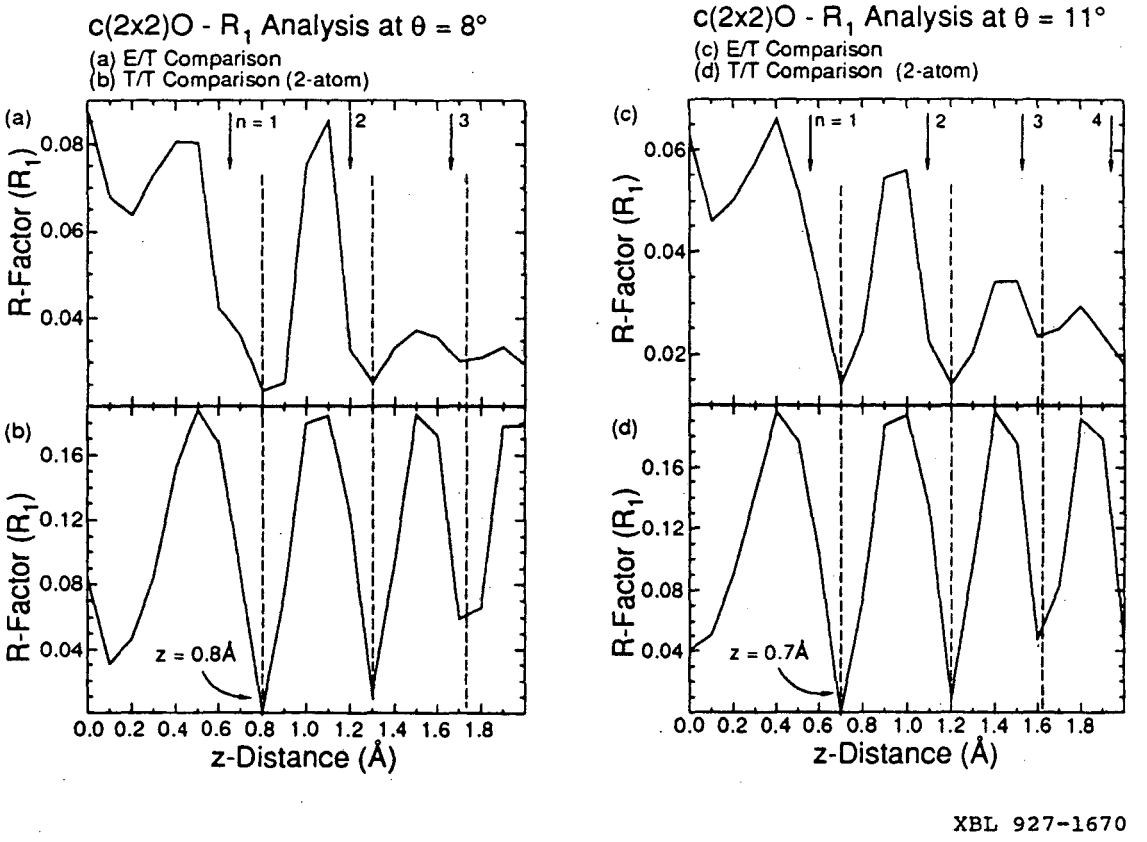
c(2x2)O - R1 Analysis at θ = 8°
(a) E/T Comparison
(b) T/T Comparison (2-atom)
c(2x2)O - R1 Analysis at θ = 11°
(c) E/T Comparison
(d) T/T Comparison (2-atom)
R-Factor (R1)
z-Distance (Å)
n = 1
2
3
4
z = 0.8Å
z = 0.7Å
XBL 927-1670

Figure 19

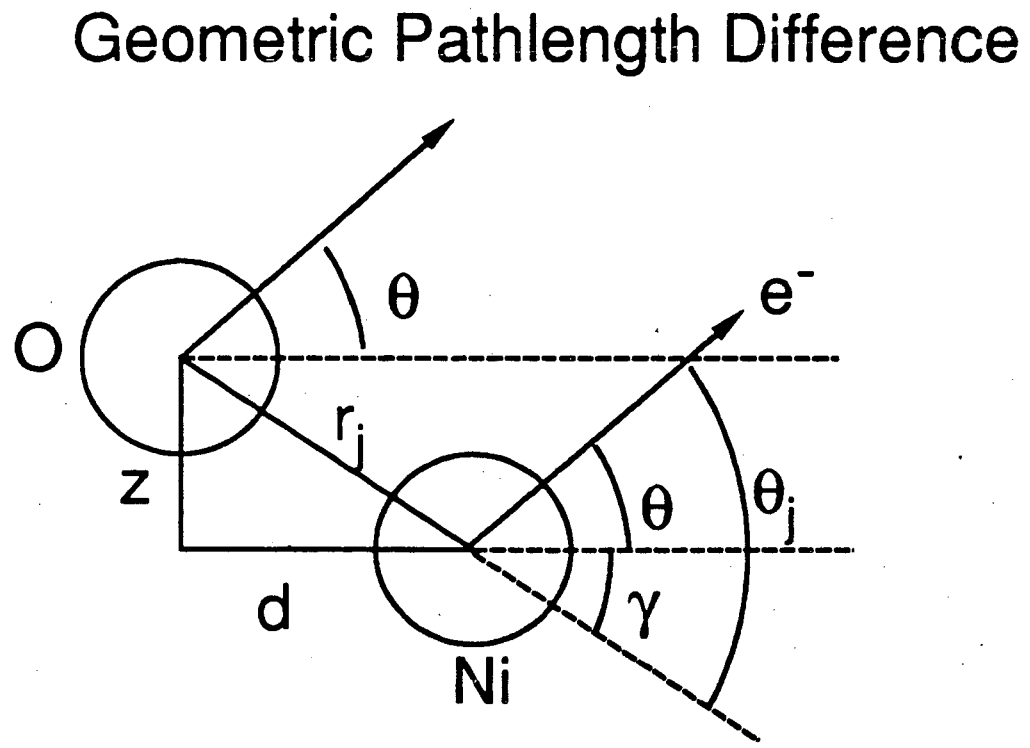
Geometric Pathlength Difference
O
θ
e⁻
r_j
z
θ
θ_j
d
γ
Ni
XBL 927-1671

Figure 20

LAWRENCE BERKELEY LABORATORY
UNIVERSITY OF CALIFORNIA
TECHNICAL INFORMATION DEPARTMENT
BERKELEY, CALIFORNIA 94720